Supporting Information

High-Stability Pillar-Layered Zn/ZnCd-MOFs with Optimized Pores for Efficient Methane Purification

Ya-Nan Guo,[a] Xiao-Yan Zhu,[a] Zi-Qian Zhou,[a] Liang Song,[a] Xiao-Hong Xiong,[b] Huan-Huan Sun,[a] Cheng-Xia Chen,[a] Ji-Jun Jiang,[a] Dieter Fenske,[a,c] Hong-Yan Chen,[a] Zhang-Wen Wei,*[a] and Cheng-Yong Su*[a]

a Y.-N. Guo, X.-Y. Zhu, Z.-Q. Zhou, L. Song, H.-H. Sun, C.-X. Chen, J.-J. Jiang, D. Fenske, H.-Y. Chen, Z.-W. Wei, C.-Y. Su

MOE Laboratory of Bioinorganic and Synthetic Chemistry, GBRCE for Functional Molecular Engineering, LIFM, IGCME, School of Chemistry, Sun Yat-Sen University. Guangzhou 510006, China

E-mail: weizhw3@mail.sysu.edu.cn; cesscy@mail.sysu.edu.cn

b X.-H. Xiong

Department of Chemistry and Chemical Engineering, Key Laboratory for Preparation and Application of Ordered Structural Materials of Guangdong Province, Shantou University, Shantou, 515063, China

c D. Fenske

Institute of Nanotechnology (INT) and Karlsruhe Nano Micro Facility (KNMF), Karlsruhe Institute of Technology (KIT), 76344 Eggenstein-Leopoldshafen, Germany

Table of Contents

S1. Materials and Instrumentation

All reagents and solvents were obtained from commercial sources and used without further purification. Scanning Electron Microscopy (SEM) images were record with a field emission SEM (FESEM, Hitachi, SU8010, Japan) operated at an electron acceleration energy of 10 kV and 9.8 μA. The morphology, structure and metal elements of the prepared samples were analyzed using a FESEM and an energy dispersive spectrometer (EDX, Oxford-Honeywell Inca XMax50). Powder X-ray diffraction (PXRD) were recorded ranging from 2 ° to 50 ° at room temperature on a RigakuSmartLab diffractometer (Bragg-Brentano geometry, Cu Kα1 radiation, λ = 1.54056 Å) at 40 kV and 15 mA. Thermogravimetric analysis (TGA) was performed on a NETZSCH TG209 system in nitrogen and under 1 atm of pressure at a heating rate of 10 °C min^{-1}. The variable-temperature (VT-PXRD) powder data were obtained using a Rigaku SmartLab X-ray powder diffractometer. The temperature change is carried out using programmed temperature rise, with a rate of 5 °C/min. After reaching the temperature range, it is maintained for 1 minute before the test begins. The atmosphere is air. The crystalline granular samples are ground on the silicon wafer to fine powder and then spread on the sample platform. N_2 adsorption isotherms for pressures in the range of 0-1.0 bar were collected by a volumetric method using a quantachrome autosorb IQ3 gas adsorption analyzer. The samples were vacuumed at 100 °C for 10 h before the sorption examination. Gas adsorption isotherms were measured on a quantachrome Autosorb-iQ2-MP gas adsorption analyzer. The breakthrough curves were collected by a home-made instrument using a gas chromatography (FL-9790 plus) as detector.

S2. Single Crystal X-Ray Crystallography

The structures were solved by direct methods using SHELXT and refined by full-matrix least squares against F^2 using the SHELXL programs.[1] Hydrogen atoms were placed in

geometrically calculated positions and included in the refinement process using riding model with isotropic thermal parameters: Uiso(H) = 1.2 Ueq(-CH). All the electrons of disordered solvent molecules which cannot be determined, are removed by SQUEEZE routine of PLATON program or the similar solvent-mask routine of Olex2 program.[2]

Table S1. Crystal data and structure refinement for LIFM-260/261.

Compound	**LIFM-260**	**LIFM-261**
CCDC No.	2439981	2439978
Empirical formula	$C_{43}H_{50}N_4O_{12}Zn_2$	$C_{43}H_{50}CdN_4O_{12}Zn$
Formula weight	945.61	992.64
Temperature (K)	292.82(13)	250.00(10)
Crystal system	triclinic	triclinic
Space group	*P-1*	*P-1*
a (Å)	10.6473(7)	10.5951(6)
b (Å)	14.9576(8)	14.8657(9)
c (Å)	16.3809(10)	16.4781(9)
α (deg)	64.547(6)	64.787(6)
β (deg)	72.669(6)	72.610(5)
γ (deg)	75.980(5)	76.868(5)
Volume (Å^3)	2228.8(3)	2225.7(3)
Z	2	2
ρ_{calc} (g cm^{-3})	1.409	1.481
μ (mm^{-1})	1.868	5.035
Index ranges	$-9 \le h \le 12$, $-13 \le k \le 18$, $-19 \le l \le 20$	$-12 \le h \le 7$, $-18 \le k \le 15$, $-19 \le l \le 18$
Reflections collected	15482	14804
Independent reflections	8474 [Rint = 0.0313, Rsigma = 0.0405]	8406 [Rint = 0.0267, Rsigma = 0.0223]
Data/restraints/ parameters	8474/605/577	8406/599/577
Goodness-of-fit on F^2	1.030	1.030
Final R indexes [I>=2σ (I)]	R_1= 0.0517, wR_2= 0.1483	R_1= 0.0583, wR_2= 0.1828
Final R indexes [all data]	R_1= 0.0675, wR_2= 0.1630	R_1= 0.0589, wR_2= 0.1835
Largest diff. peak/hole (e Å^{-3})	0.78/-0.69	1.58/-1.67

Table S2. Crystal data and structure refinement for LIFM-262/263.

Compound	**LIFM-262**	**LIFM-263**
CCDC No.	2439995	2439992
Empirical formula	$C_{40}H_{30}N_2O_6Zn$	$C_{66}H_{44}N_2O_{13}Zn_3$
Formula weight	700.03	1269.14
Temperature (K)	250.00(10)	99.99(10)
Crystal system	monoclinic	triclinic
Space group	*P2₁/n*	*P-1*
a (Å)	9.4054(5)	16.1220(5)
b (Å)	28.0637(10)	16.7489(5)
c (Å)	15.6060(8)	18.2600(4)
α (deg)	90	86.169(2)
β (deg)	100.435(6)	76.092(2)
γ (deg)	90	61.238(3)
Volume (Å³)	4051.1(3)	4188.7(2)
Z	4	2
ρ_{calc} (g cm^{-3})	1.148	1.006
μ (mm^{-1})	1.192	1.391
Index ranges	$-7 \le h \le 7$, $-23 \le k \le 16$, $-9 \le l \le 12$	$-13 \le h \le 13$, $-13 \le k \le 13$, $-15 \le l \le 15$
Reflections collected	3307	9286
Independent reflections	2053 [R_{int}= 0.0138, R_{sigma}= 0.0214]	4428 [R_{int}= 0.0518, R_{sigma}= 0.0473]
Data/restraints/ parameters	2053/753/503	4428/1359/750
Goodness-of-fit on F²	1.079	1.059
Final R indexes [I>=2σ (I)]	R_1= 0.0684, wR_2= 0.1690	R_1= 0.0666, wR_2= 0.1734
Final R indexes [all data]	R_1= 0.0724, wR_2= 0.1726	R_1= 0.0693, wR_2= 0.1756
Largest diff. peak/hole (e Å^{-3})	0.59/-0.38	0.57/-0.62

Table S3. Crystal data and structure refinement for LIFM-264/265.

Compound	LIFM-264	LIFM-265
CCDC No.	2439994	2439991
Empirical formula	$C_{68}H_{48}CdN_2O_{13}Zn_2$	$C_{274}H_{200}Cd_8N_{10}O_{60}Zn_4$
Formula weight	1344.22	5753.11
Temperature (K)	260(15)	100.00(10)
Crystal system	triclinic	monoclinic
Space group	*P-1*	$P2_1/n$
a (Å)	16.6806(7)	17.7370(7)
b (Å)	16.6921(6)	28.9138(12)
c (Å)	20.2376(5)	32.2412(11)
α (deg)	71.395(3)	90
β (deg)	76.477(3)	94.410(3)
γ (deg)	60.148(4)	90
Volume (Å^3)	4612.4(3)	16485.8(11)
Z	2	2
ρ_{calc} (g cm^{-3})	0.968	1.159
μ (mm^{-1})	2.798	4.876
Index ranges	$-13 \le h \le 13$, $-13 \le k \le 13$, $-16 \le l \le 16$	$-14 \le h \le 14$, $-23 \le k \le 24$, $-26 \le l \le 26$
Reflections collected	16431	61665
Independent reflections	5532 [Rint = 0.0370, Rsigma = 0.0341]	9990 [R_{int} = 0.0860, R_{sigma} = 0.0575]
Data/restraints/ parameters	5532/830/817	9990/1784/1569
Goodness-of-fit on F^2	1.068	1.129
Final R indexes [I>=2σ (I)]	R_1= 0.0537, wR_2= 0.1451	R_1= 0.1411, wR_2= 0.3214
Final R indexes [all data]	R_1= 0.0597, wR_2= 0.1545	R1 = 0.1774, wR2 = 0.3466
Largest diff. peak/hole (e Å^{-3})	1.18/-0.61	4.13/-1.40

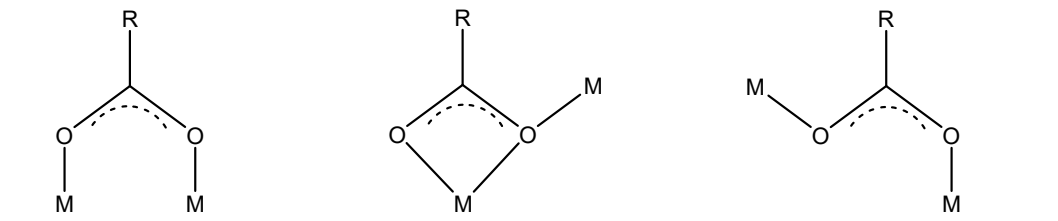

(a) *syn-syn* μ_2-η^1:η^1 (b) μ_2-η^2:η^1 (c) *syn-anti* μ_2-η^1:η^1

Figure S1. Selected coordination motifs for carboxylate-containing ligands.[3,4]

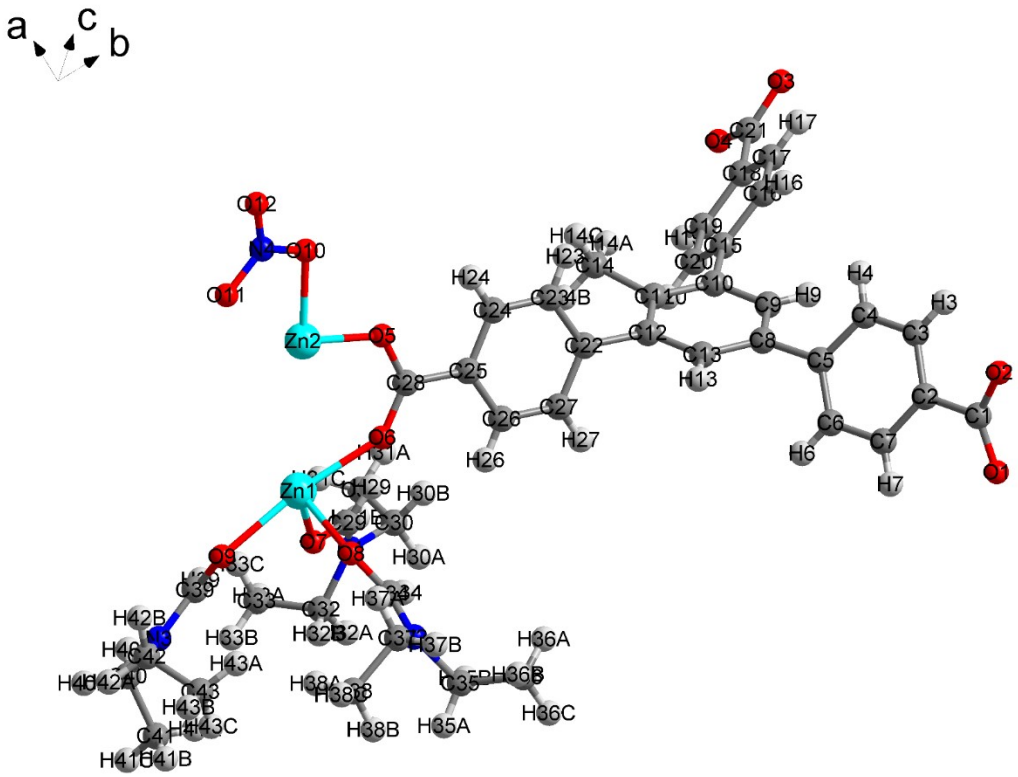

Figure S2. The asymmetric unit of LIFM-260.

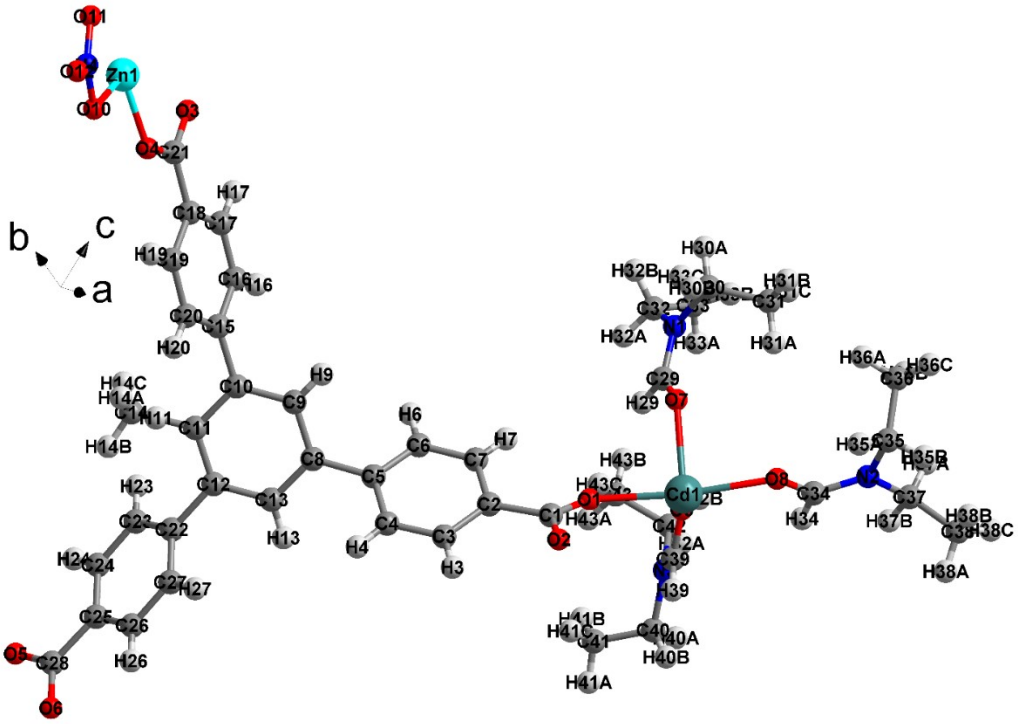

Figure S3. The asymmetric unit of LIFM-261.

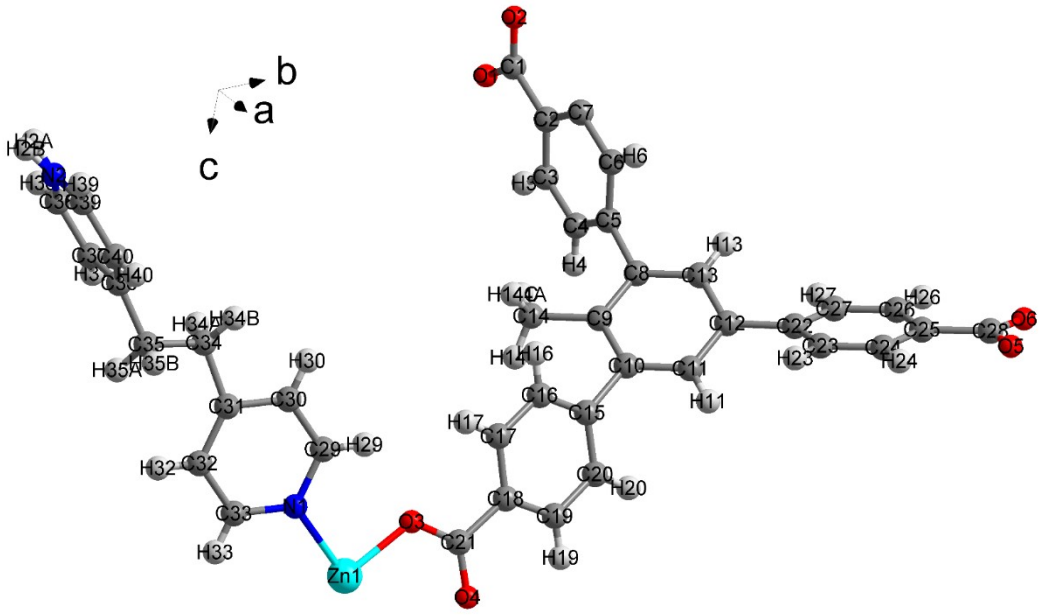

Figure S4. The asymmetric unit of LIFM-262.

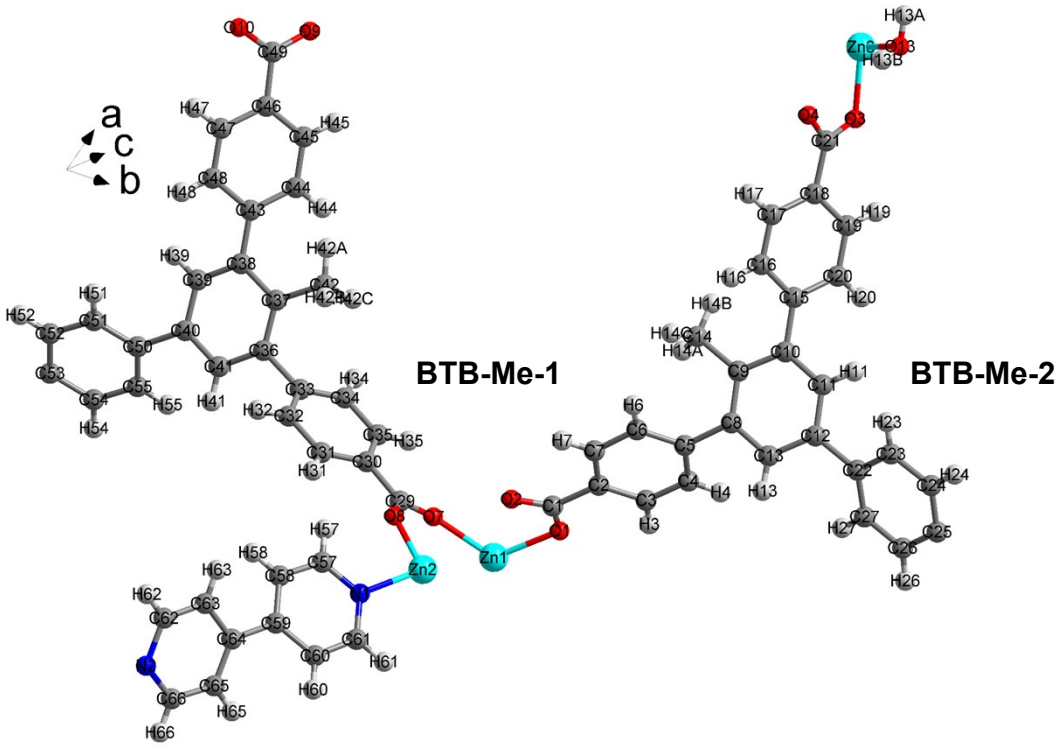

Figure S5. The asymmetric unit of LIFM-263.

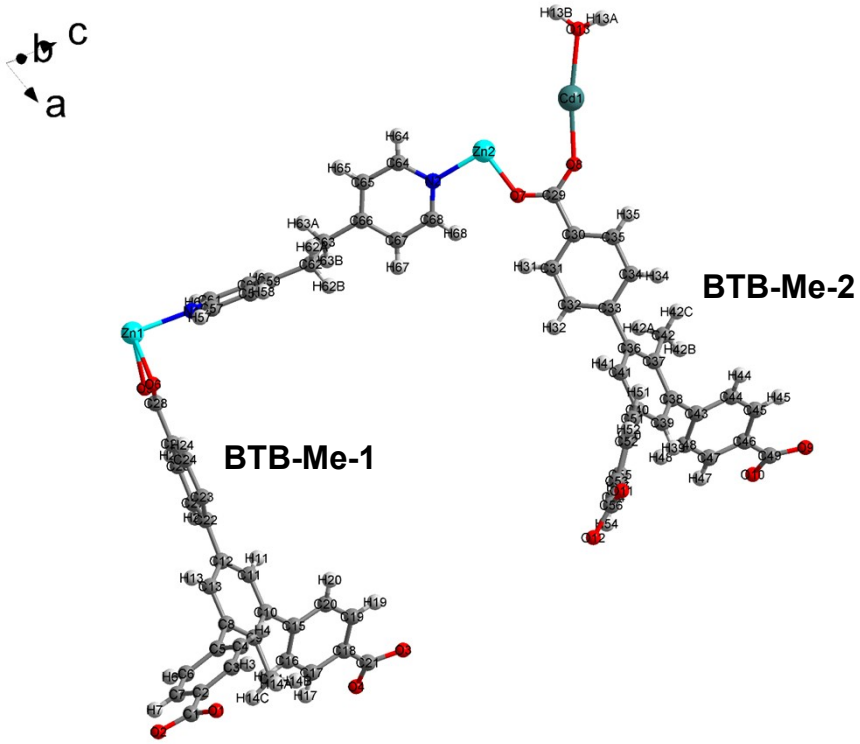

Figure S6. The asymmetric unit of LIFM-264.

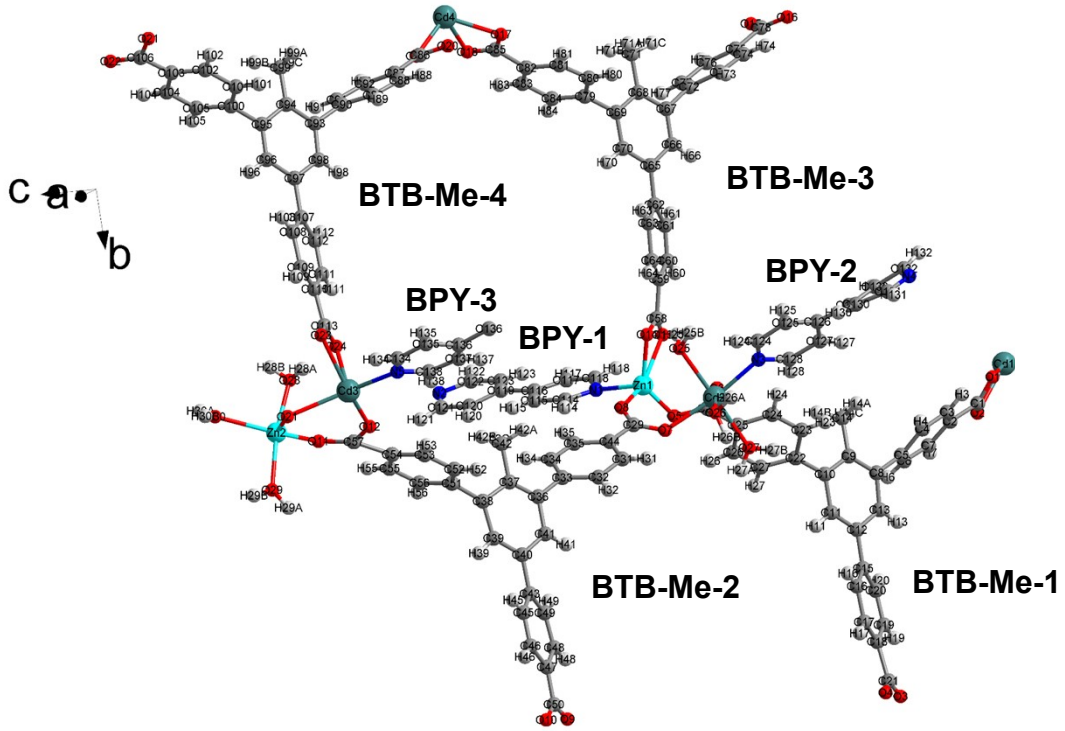

Figure S7. The asymmetric unit of LIFM-265.

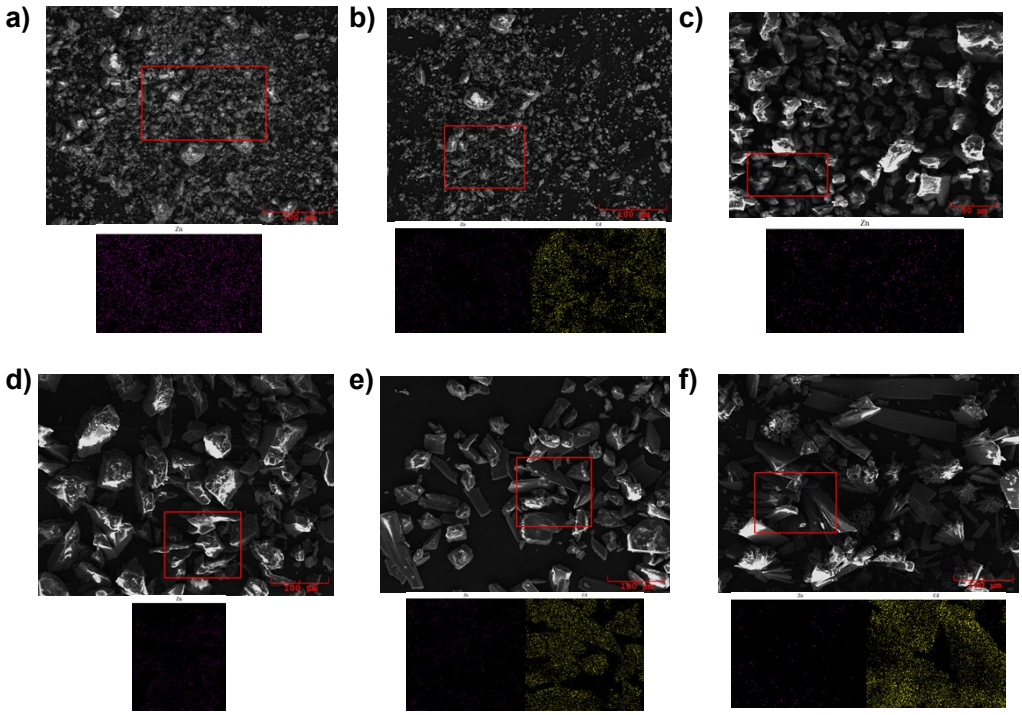

Figure S8. FESEM image and EDX mapping of a) Zn element on LIFM-260, b) Zn, Cd elements on LIFM-261, c) Zn element on LIFM-262, d) Zn element on LIFM-263, e) Zn, Cd elements on LIFM-264, f) Zn, Cd elements on LIFM-265.

S3. Powder X-Ray Diffraction

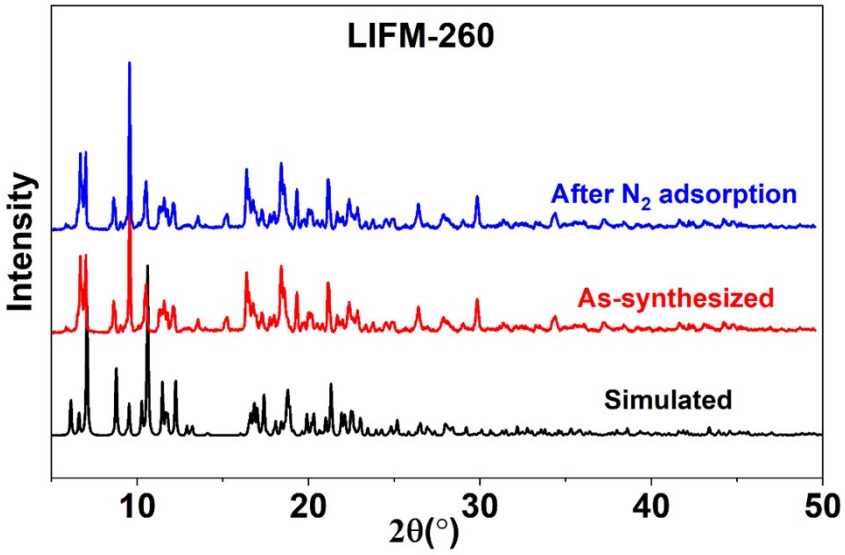

Figure S9. The simulated and experimental PXRD patterns of LIFM-260.

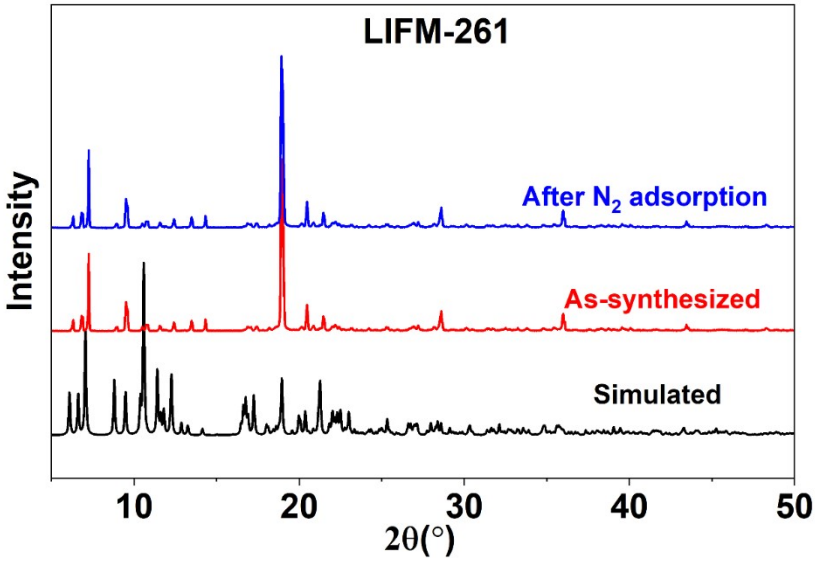

Figure S10. The simulated and experimental PXRD patterns of LIFM-261.

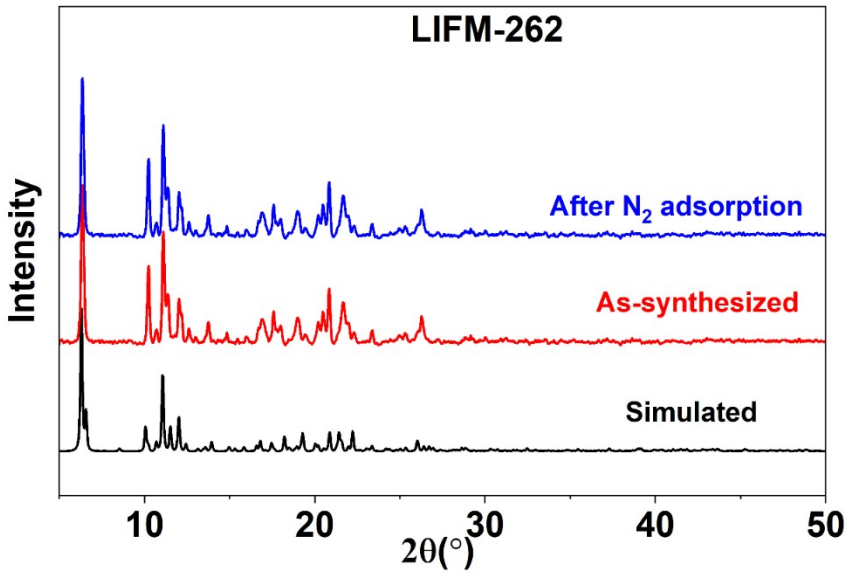

Figure S11. The simulated and experimental PXRD patterns of LIFM-262.

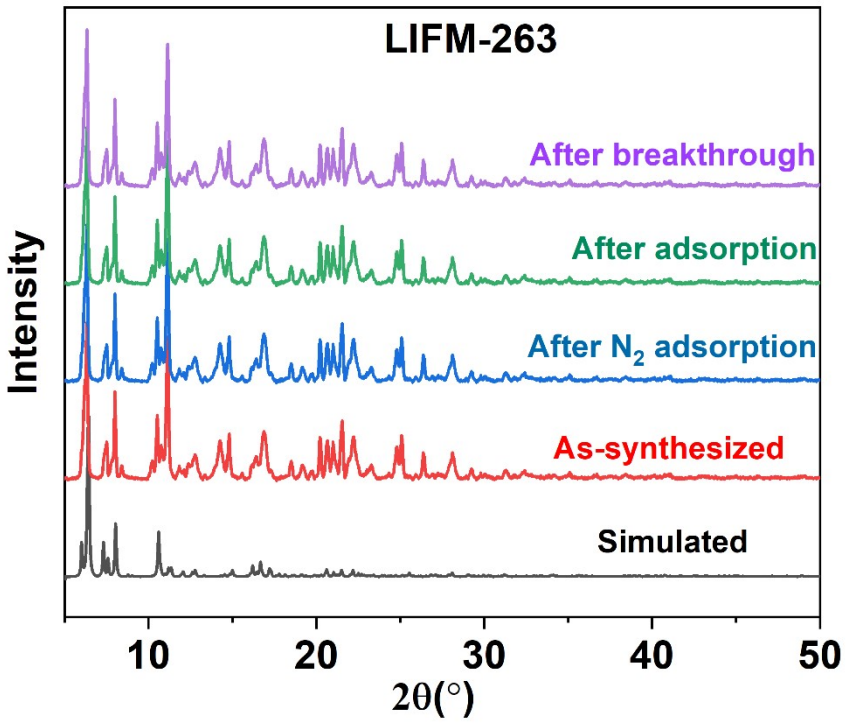

Figure S12. The simulated and experimental PXRD patterns of LIFM-263.

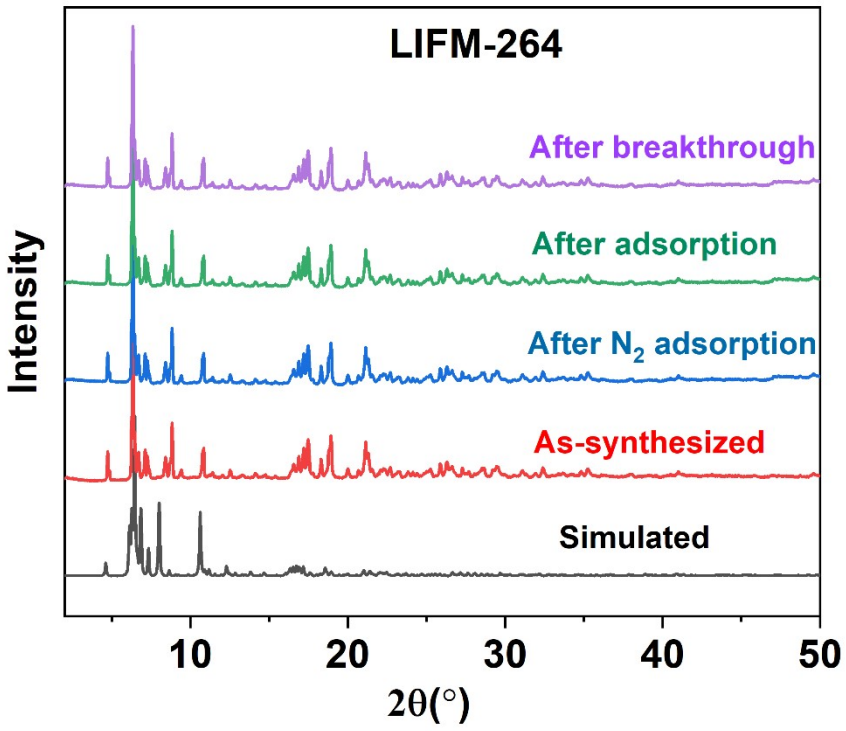

Figure S13. The simulated and experimental PXRD patterns of LIFM-264.

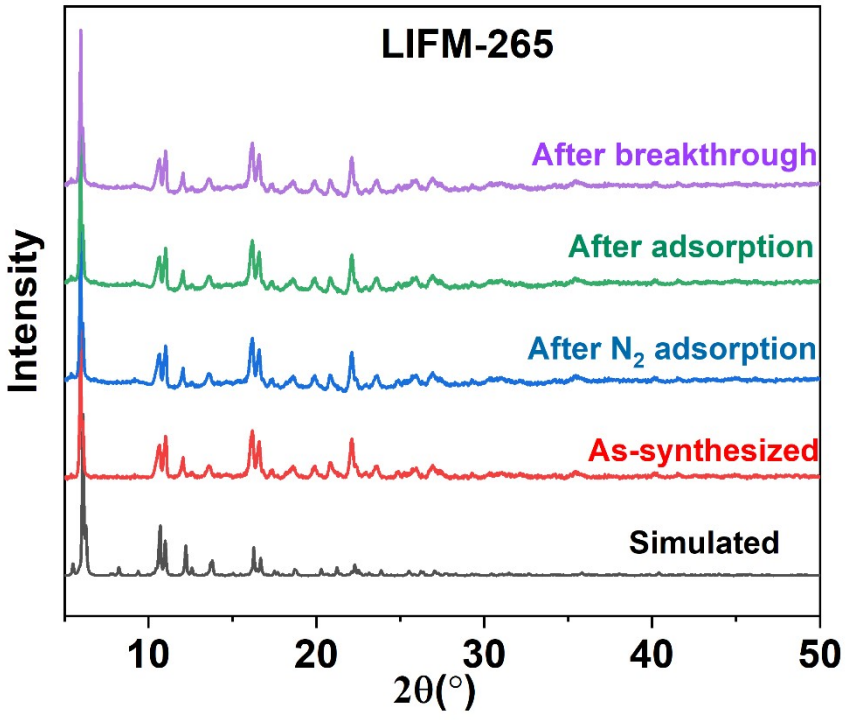

Figure S14. The simulated and experimental PXRD patterns of LIFM-265.

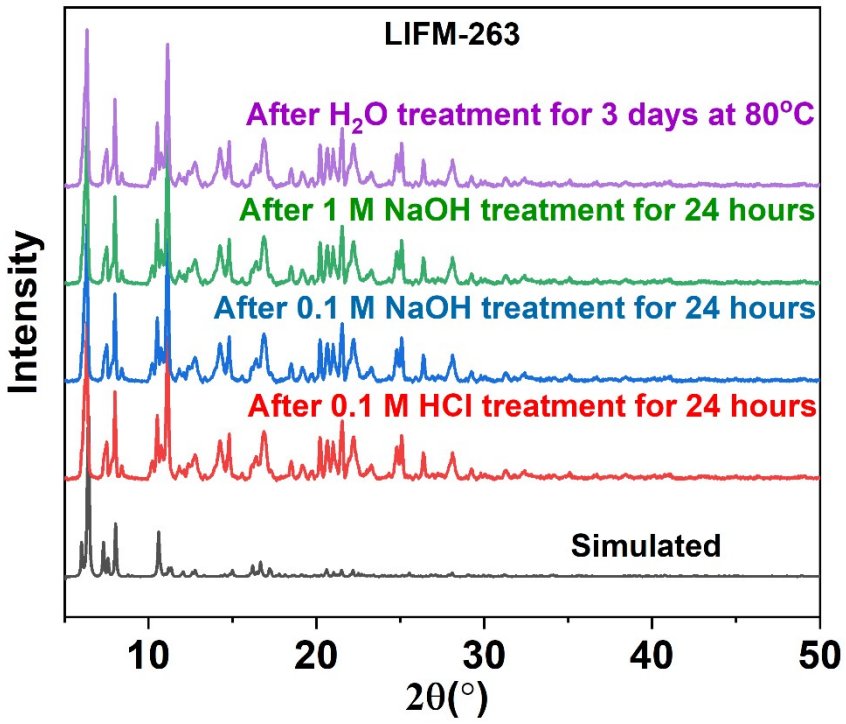

Figure S15. PXRD patterns of LIFM-263 immersed in 0.1 M HCl, 0.1 M NaOH, 1 M NaOH and 80 °C water for 3 days, respectively.

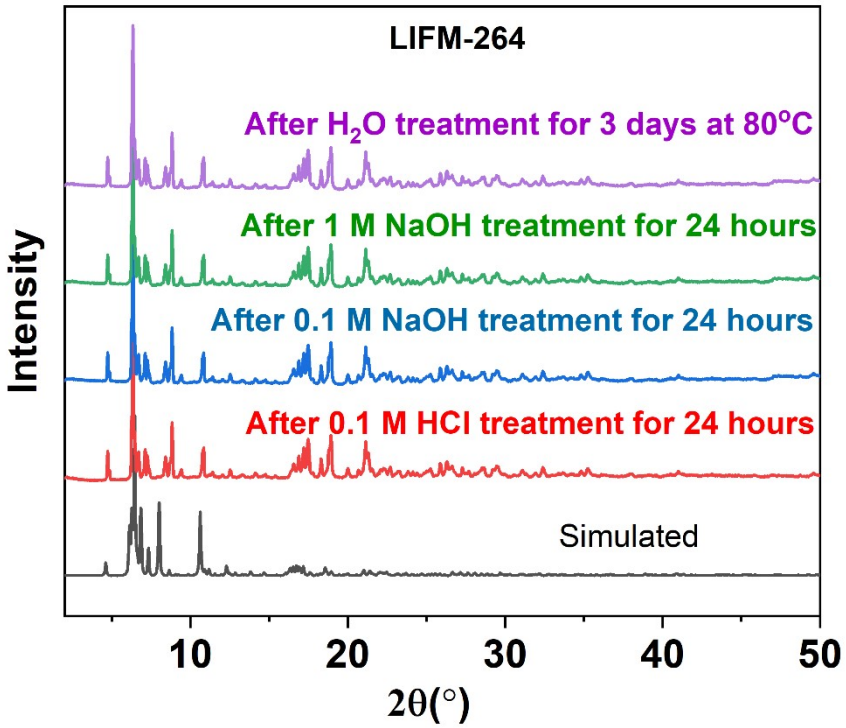

Figure S16. PXRD patterns of LIFM-264 immersed in 0.1 M HCl, 0.1 M NaOH, 1 M NaOH and 80 °C water for 3 days, respectively.

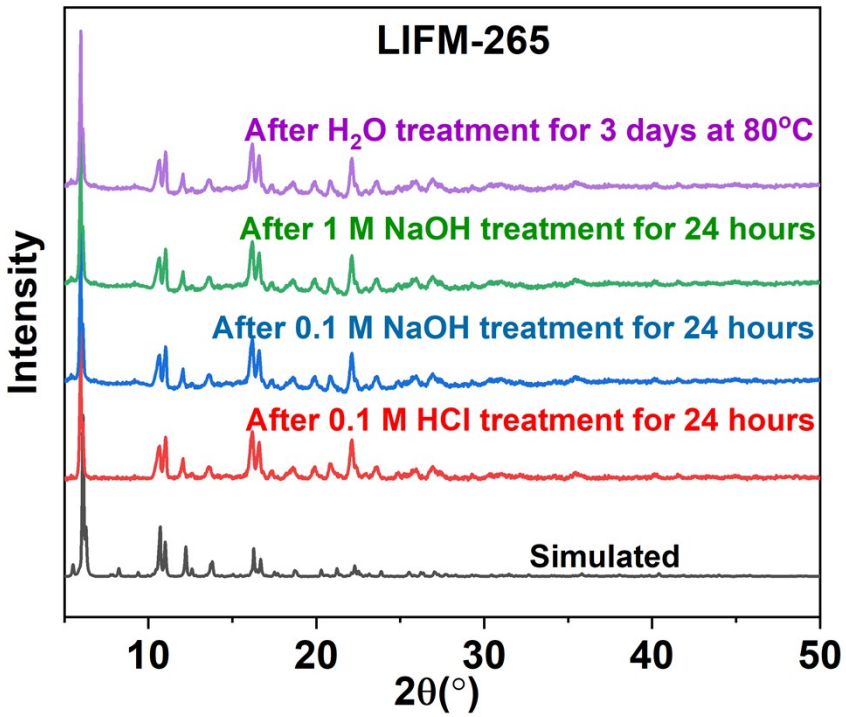

Figure S17. PXRD patterns of LIFM-265 immersed in 0.1 M HCl, 0.1 M NaOH, 1 M NaOH and 80 °C water for 3 days, respectively.

.

S4. Thermal Stability Analysis

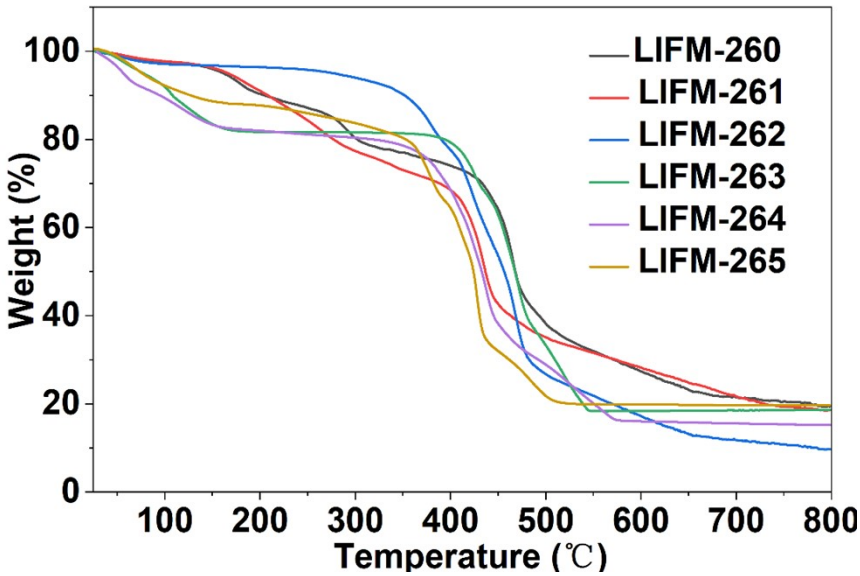

Figure S18. The TGA of as-synthesized MOFs.

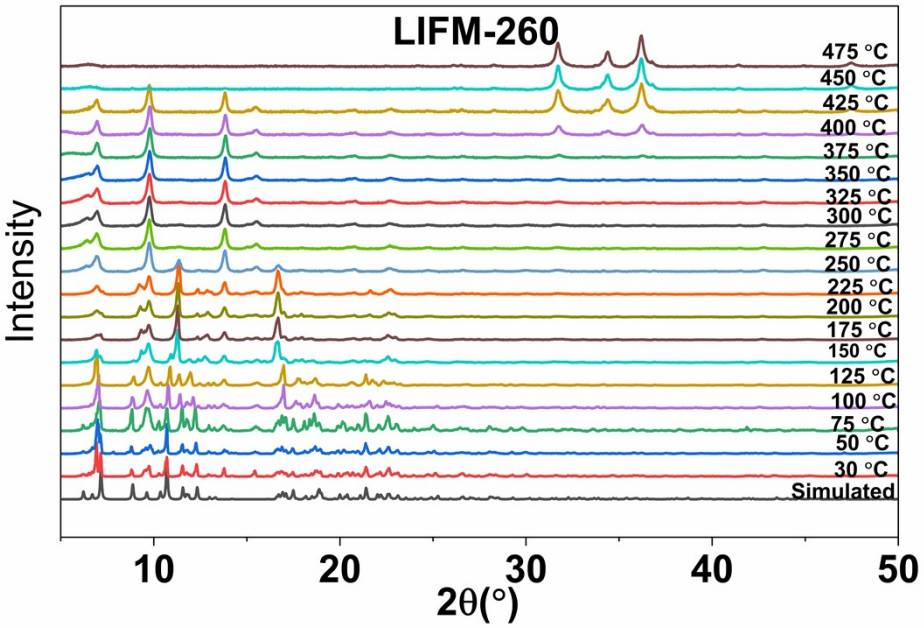

Figure S19. The VT-PXRD patterns of LIFM-260.

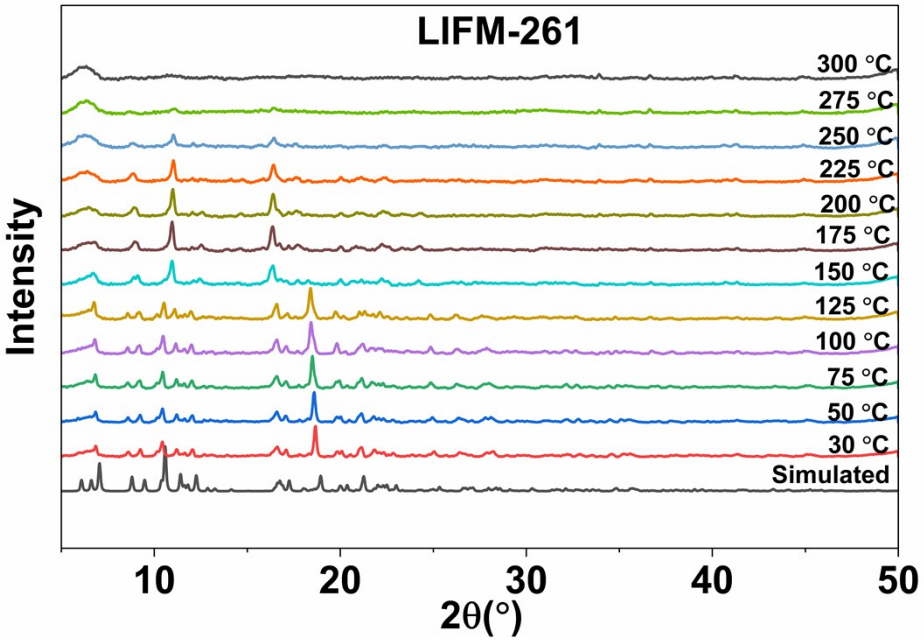

Figure S20. The VT-PXRD patterns of LIFM-261.

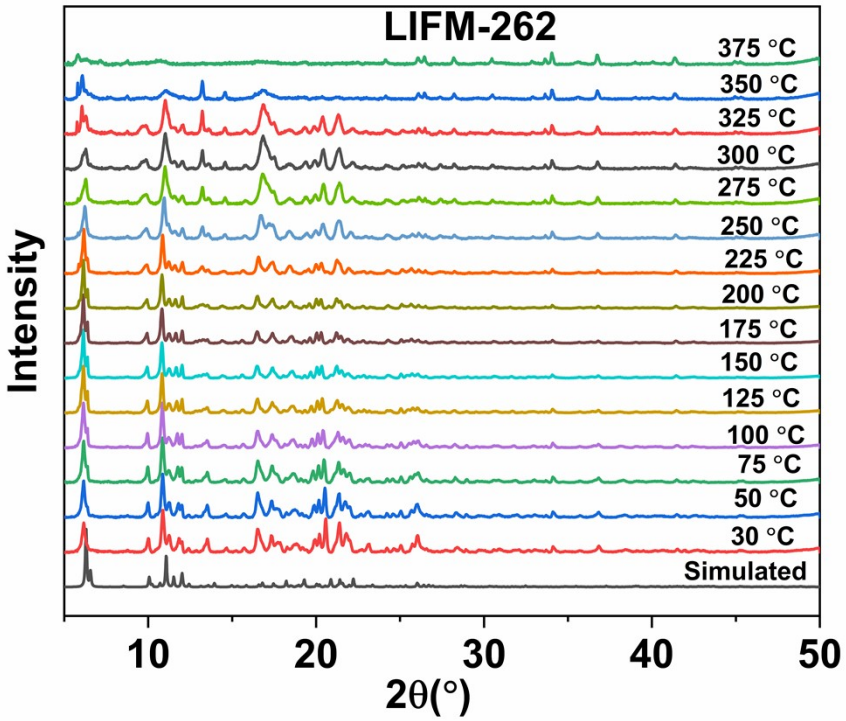

Figure S21. The VT-PXRD patterns of LIFM-262.

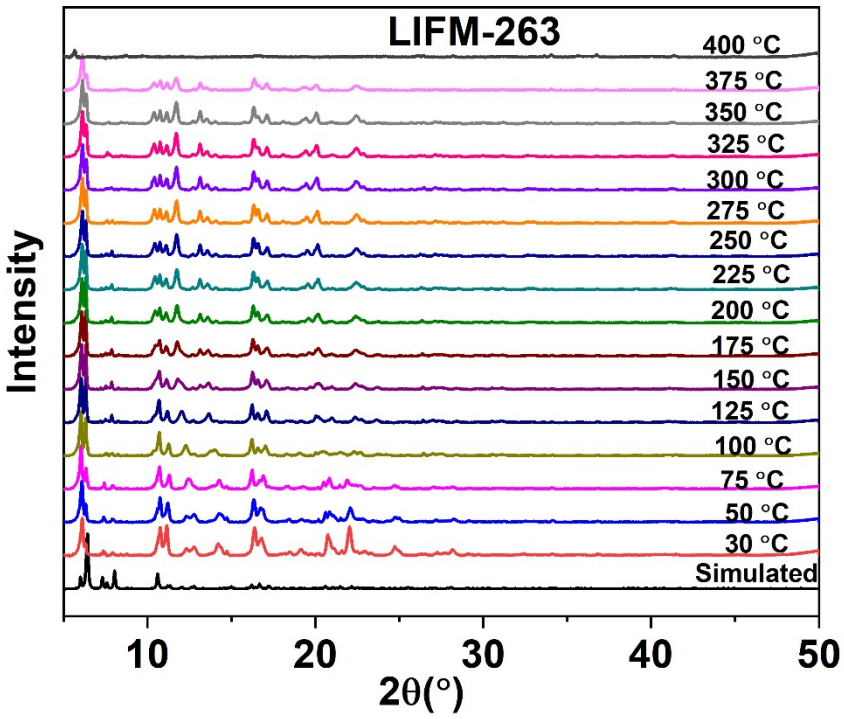

Figure S22. The VT-PXRD patterns of LIFM-263.

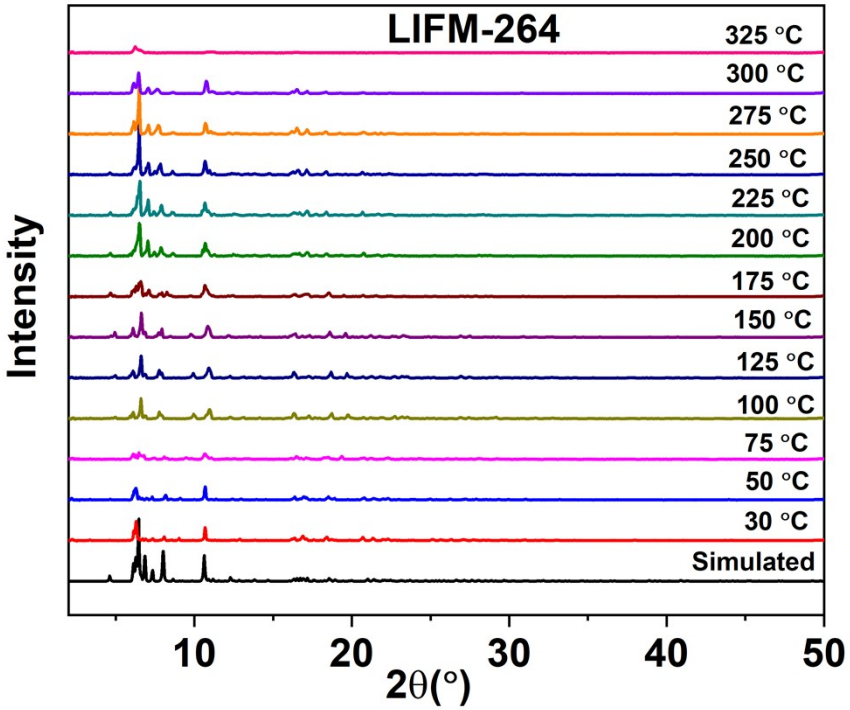

Figure S23. The VT-PXRD patterns of LIFM-264.

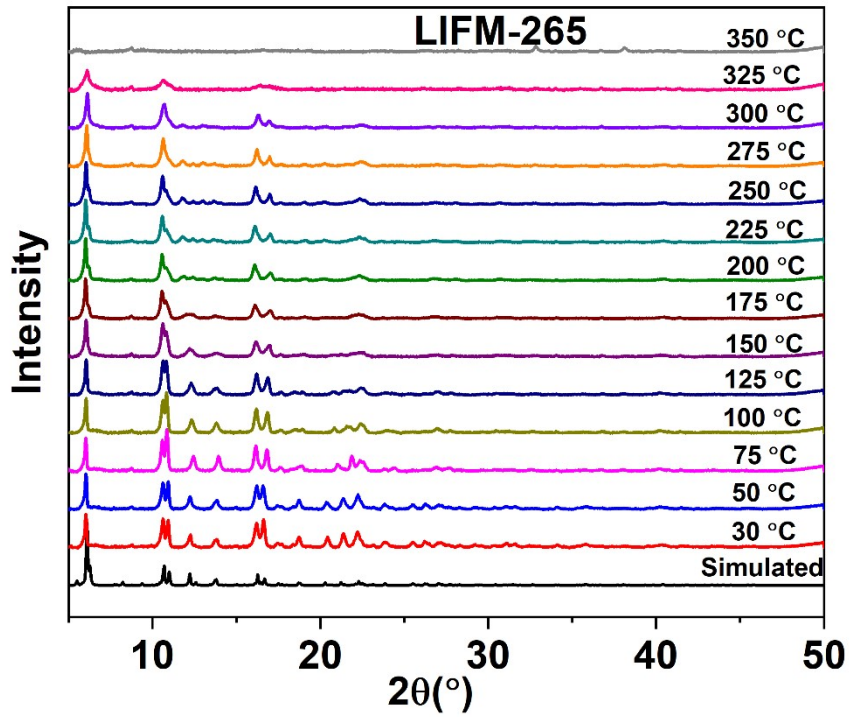

Figure S24. The VT-PXRD patterns of LIFM-265.

S5. Porosity Characterization

N_2 sorption isotherm at 77 K: before gas sorption experiments, the as-synthesized samples of the five MOFs were immersed in ether for 3 days, during which the solvent was decanted and freshly replenished 3 times a day. The solvent-exchanged samples of the MOFs were activated under vacuum at 100 °C for 10 hours. N_2 adsorption isotherms for pressures in the range of 0-1.0 bar were collected by a volumetric method using a quantachrome autosorb IQ3 gas adsorption analyzer. The BET calculation fittings are plotted in Figure S24-S26. The porosity parameters of MOFs are summarized in **Table S4**. The model settings for calculating pore distributions of the MOFs are as follows: 1) LIFM-263: N_2 at 77 K on carbon (slit pore, QSDFT equilibrium model); 2) LIFM-264: N_2 at 77 K on carbon (slit pore, QSDFT equilibrium model); 3) LIFM-265: N_2 at 77 K on carbon (slit pore, QSDFT equilibrium model).

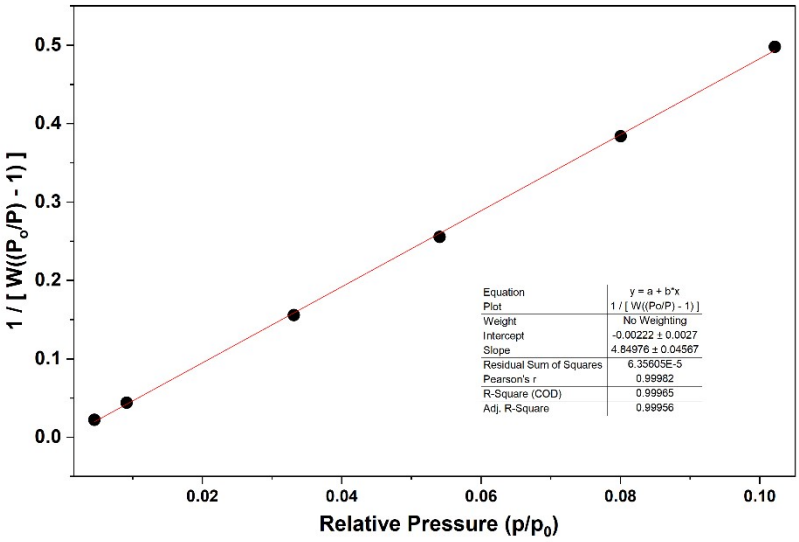

Figure S25. Plot of the linear region on the N_2 isotherm of LIFM-263 for the BET equation.

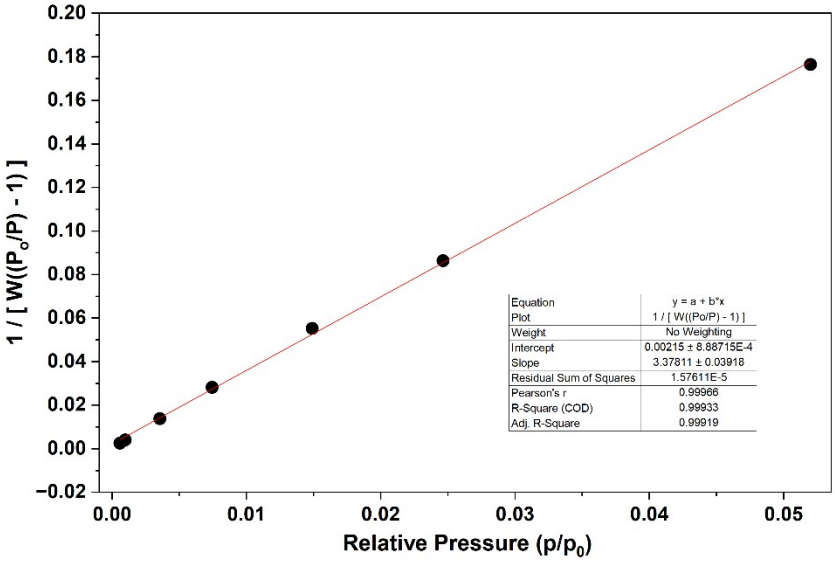

Figure S26. Plot of the linear region on the N_2 isotherm of LIFM-264 for the BET equation.

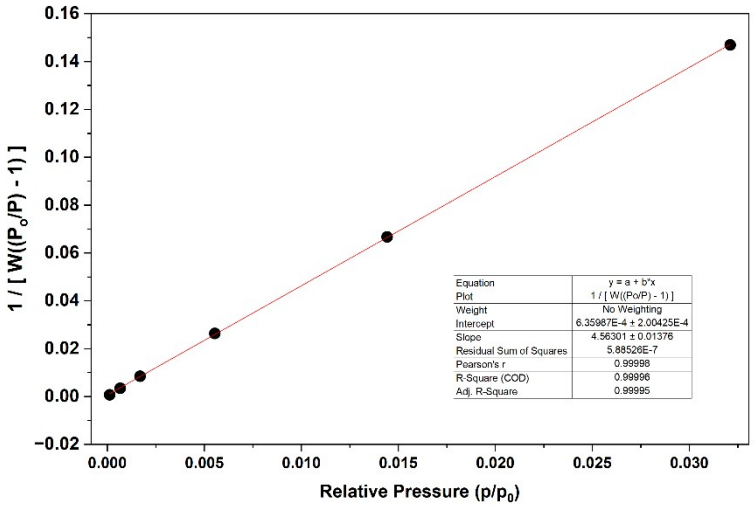

Figure S27. Plot of the linear region on the N_2 isotherm of LIFM-265 for the BET equation.

Table S4. The porosity parameters of the three MOFs.

MOF	BET surface area ($m^2\ g^{-1}$)	Total pore volume ($cm^3\ g^{-1}$)	Pore size (nm)
LIFM-263	718	0.30	0.57,0.72
LIFM-264	1030	0.43	0.57,0.72,1.25
LIFM-265	763	0.31	0.72

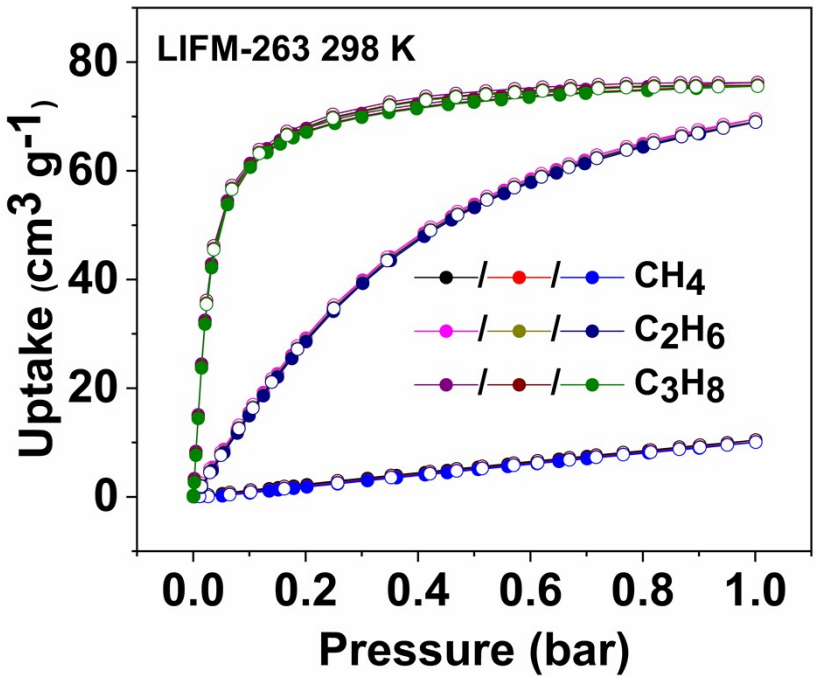

Figure S28. Adsorption–desorption cycling of CH_4, C_2H_6, and C_3H_8 on LIFM-263 at 298 K.

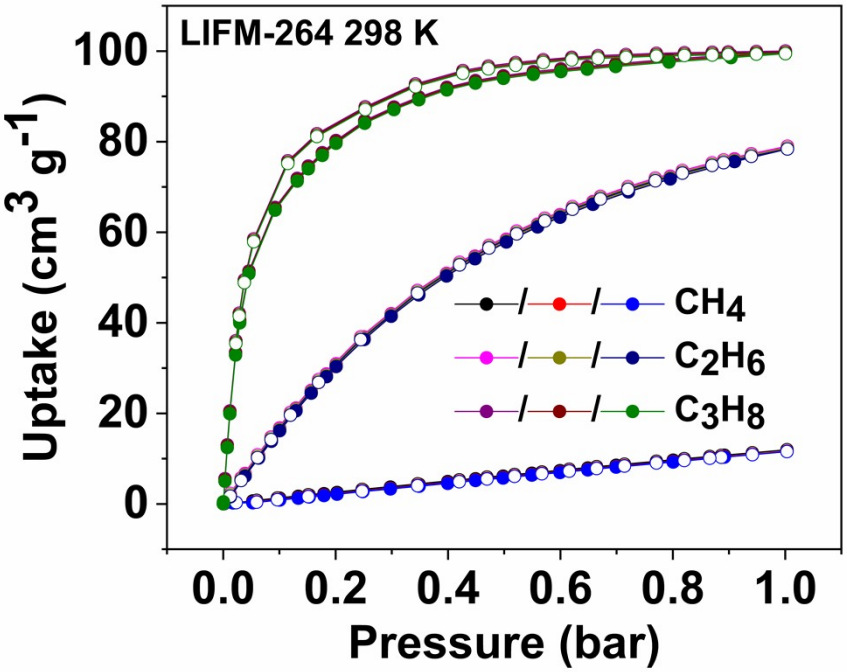

Figure S29. Adsorption–desorption cycling of CH_4, C_2H_6, and C_3H_8 on LIFM-264 at 298 K.

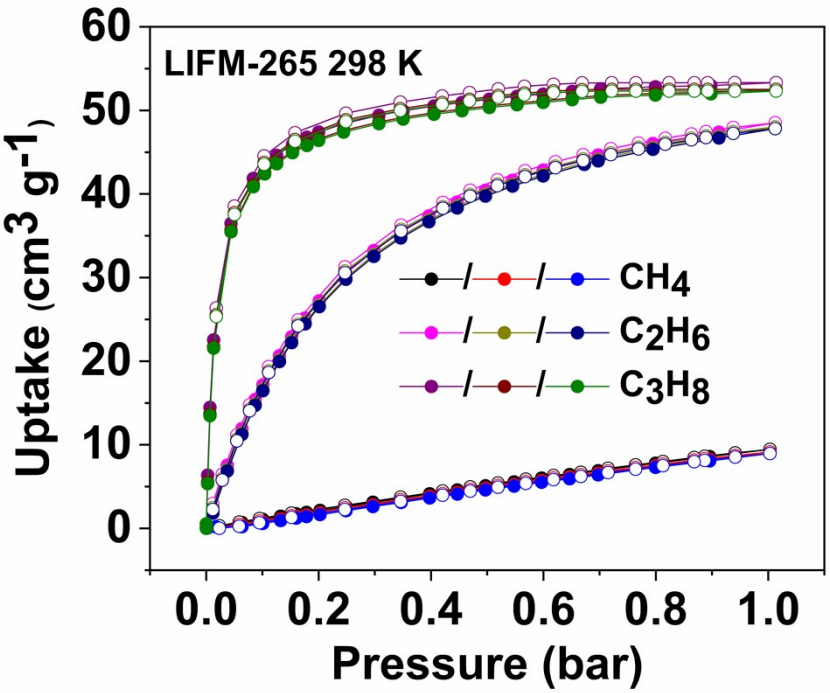

Figure S30. Adsorption–desorption cycling of CH_4, C_2H_6, and C_3H_8 on LIFM-265 at 298 K.

S6. Calculations of Q_{st}

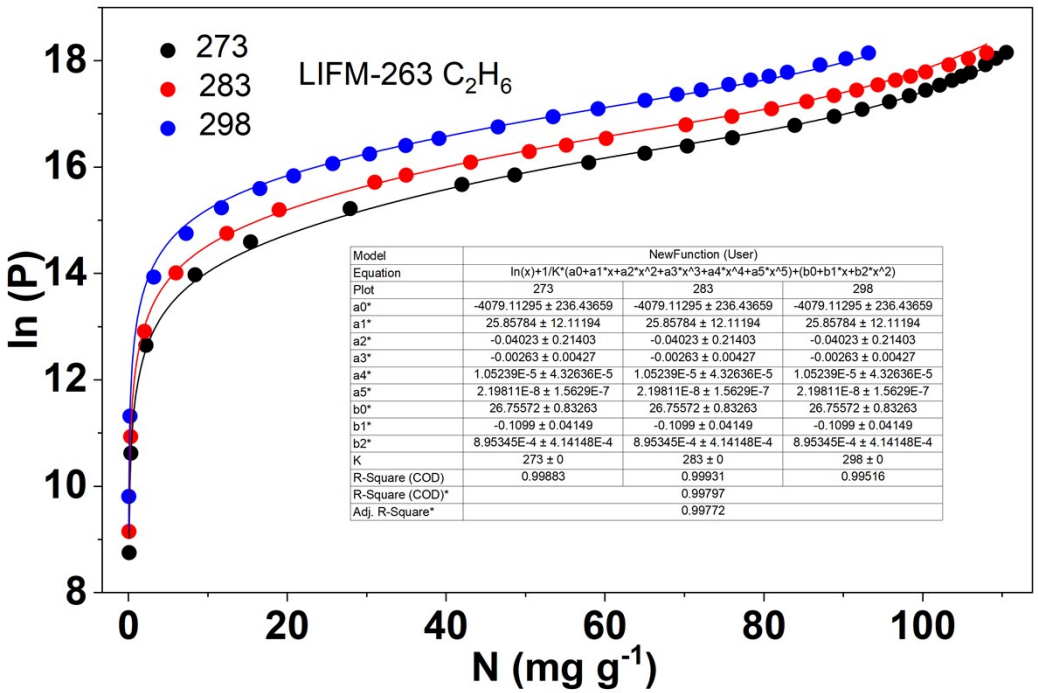

Model	NewFunction (User)		
Equation	ln(x)+1/K*(a0+a1*x+a2*x^2+a3*x^3+a4*x^4+a5*x^5)+(b0+b1*x+b2*x^2)		
Plot	273	283	298
a0*	-4079.11295 ± 236.43659	-4079.11295 ± 236.43659	-4079.11295 ± 236.43659
a1*	25.85784 ± 12.11194	25.85784 ± 12.11194	25.85784 ± 12.11194
a2*	-0.04023 ± 0.21403	-0.04023 ± 0.21403	-0.04023 ± 0.21403
a3*	-0.00263 ± 0.00427	-0.00263 ± 0.00427	-0.00263 ± 0.00427
a4*	1.05239E-5 ± 4.32636E-5	1.05239E-5 ± 4.32636E-5	1.05239E-5 ± 4.32636E-5
a5*	2.19811E-8 ± 1.5629E-7	2.19811E-8 ± 1.5629E-7	2.19811E-8 ± 1.5629E-7
b0*	26.75572 ± 0.83263	26.75572 ± 0.83263	26.75572 ± 0.83263
b1*	-0.1099 ± 0.04149	-0.1099 ± 0.04149	-0.1099 ± 0.04149
b2*	8.95345E-4 ± 4.14148E-4	8.95345E-4 ± 4.14148E-4	8.95345E-4 ± 4.14148E-4
K	273 ± 0	283 ± 0	298 ± 0
R-Square (COD)	0.99883	0.99931	0.99516
R-Square (COD)*	0.99797		
Adj. R-Square*	0.99772		

Figure S31. C_2H_6 virial fitting (lines) of the adsorption isotherms (points) of LIFM-263 measured at 273 K, 283 K, and 298 K.

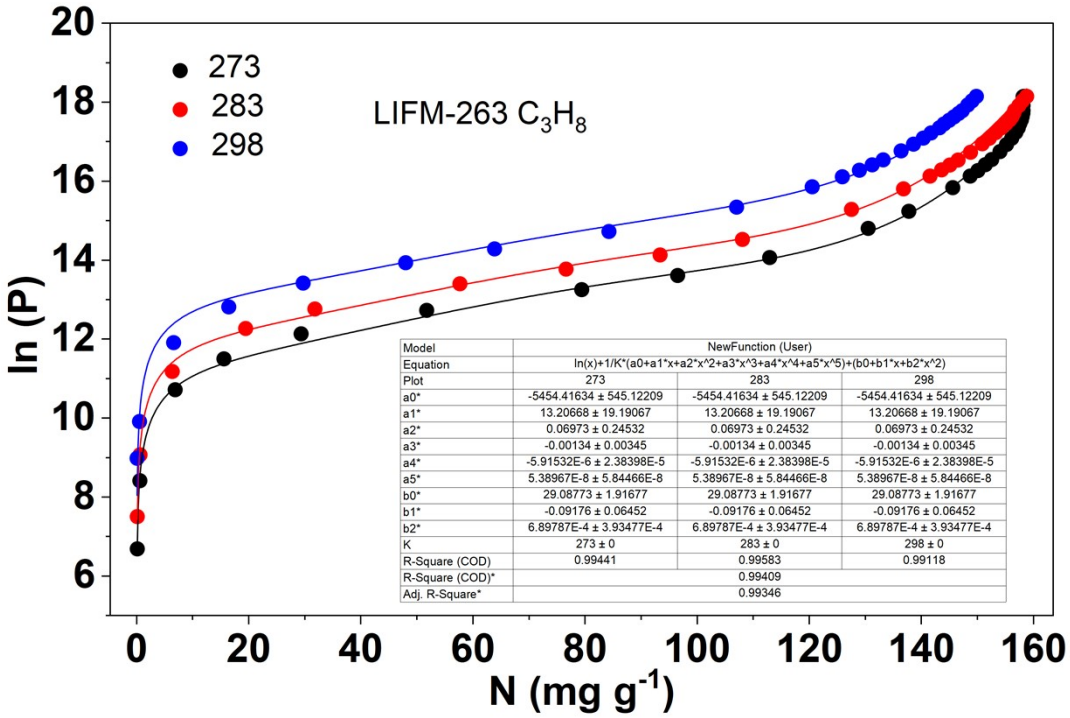

Model	NewFunction (User)		
Equation	ln(x)+1/K*(a0+a1*x+a2*x^2+a3*x^3+a4*x^4+a5*x^5)+(b0+b1*x+b2*x^2)		
Plot	273	283	298
a0*	-5454.41634 ± 545.12209	-5454.41634 ± 545.12209	-5454.41634 ± 545.12209
a1*	13.20668 ± 19.19067	13.20668 ± 19.19067	13.20668 ± 19.19067
a2*	0.06973 ± 0.24532	0.06973 ± 0.24532	0.06973 ± 0.24532
a3*	-0.00134 ± 0.00345	-0.00134 ± 0.00345	-0.00134 ± 0.00345
a4*	-5.91532E-6 ± 2.38398E-5	-5.91532E-6 ± 2.38398E-5	-5.91532E-6 ± 2.38398E-5
a5*	5.38967E-8 ± 5.84466E-8	5.38967E-8 ± 5.84466E-8	5.38967E-8 ± 5.84466E-8
b0*	29.08773 ± 1.91677	29.08773 ± 1.91677	29.08773 ± 1.91677
b1*	-0.09176 ± 0.06452	-0.09176 ± 0.06452	-0.09176 ± 0.06452
b2*	6.89787E-4 ± 3.93477E-4	6.89787E-4 ± 3.93477E-4	6.89787E-4 ± 3.93477E-4
K	273 ± 0	283 ± 0	298 ± 0
R-Square (COD)	0.99441	0.99583	0.99118
R-Square (COD)*	0.99409		
Adj. R-Square*	0.99346		

Figure S32. C_3H_8 virial fitting (lines) of the adsorption isotherms (points) of LIFM-263 measured at 273 K, 283 K, and 298 K.

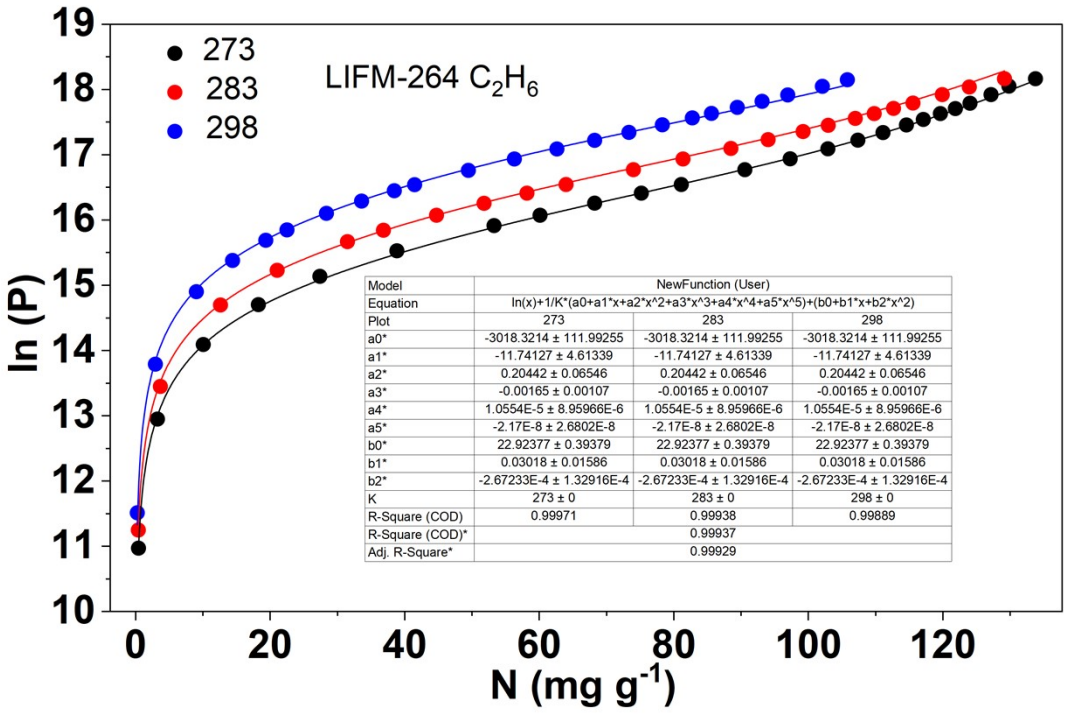

Model	NewFunction (User)		
Equation	ln(x)+1/K*(a0+a1*x+a2*x^2+a3*x^3+a4*x^4+a5*x^5)+(b0+b1*x+b2*x^2)		
Plot	273	283	298
a0*	-3018.3214 ± 111.99255	-3018.3214 ± 111.99255	-3018.3214 ± 111.99255
a1*	-11.74127 ± 4.61339	-11.74127 ± 4.61339	-11.74127 ± 4.61339
a2*	0.20442 ± 0.06546	0.20442 ± 0.06546	0.20442 ± 0.06546
a3*	-0.00165 ± 0.00107	-0.00165 ± 0.00107	-0.00165 ± 0.00107
a4*	1.0554E-5 ± 8.95966E-6	1.0554E-5 ± 8.95966E-6	1.0554E-5 ± 8.95966E-6
a5*	-2.17E-8 ± 2.6802E-8	-2.17E-8 ± 2.6802E-8	-2.17E-8 ± 2.6802E-8
b0*	22.92377 ± 0.39379	22.92377 ± 0.39379	22.92377 ± 0.39379
b1*	0.03018 ± 0.01586	0.03018 ± 0.01586	0.03018 ± 0.01586
b2*	-2.67233E-4 ± 1.32916E-4	-2.67233E-4 ± 1.32916E-4	-2.67233E-4 ± 1.32916E-4
K	273 ± 0	283 ± 0	298 ± 0
R-Square (COD)	0.99971	0.99938	0.99889
R-Square (COD)*	0.99937		
Adj. R-Square*	0.99929		

Figure S33. C_2H_6 virial fitting (lines) of the adsorption isotherms (points) of LIFM-264 measured at 273 K, 283 K, and 298 K.

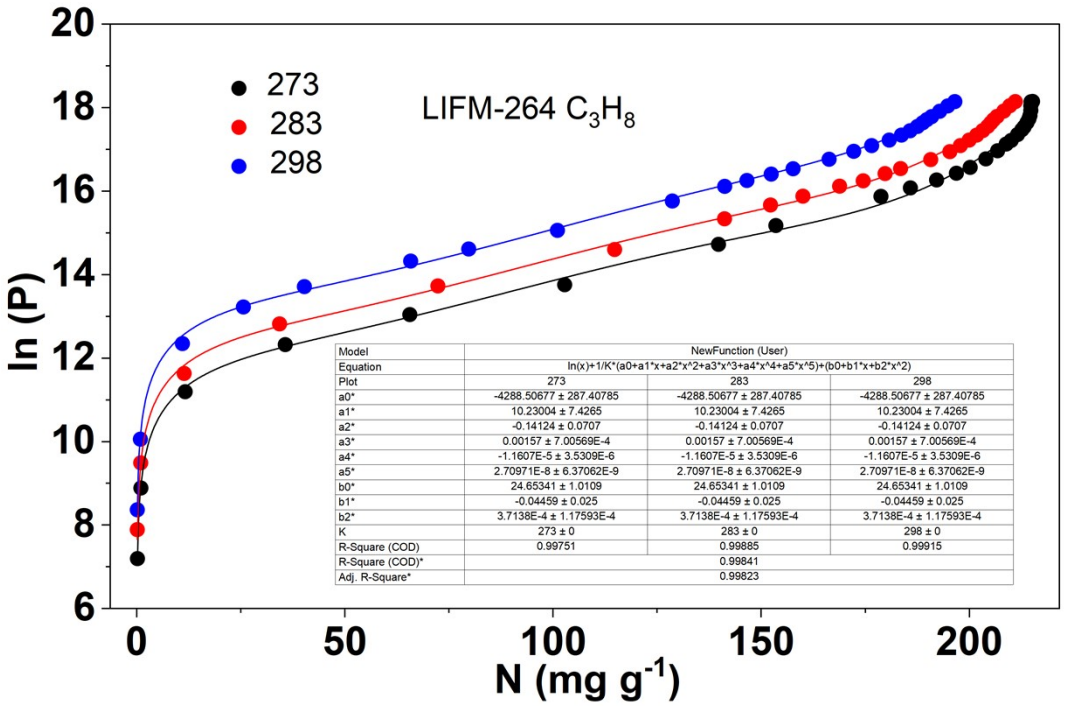

Model	NewFunction (User)		
Equation	ln(x)+1/K*(a0+a1*x+a2*x^2+a3*x^3+a4*x^4+a5*x^5)+(b0+b1*x+b2*x^2)		
Plot	273	283	298
a0*	-4288.50677 ± 287.40785	-4288.50677 ± 287.40785	-4288.50677 ± 287.40785
a1*	10.23004 ± 7.4265	10.23004 ± 7.4265	10.23004 ± 7.4265
a2*	-0.14124 ± 0.0707	-0.14124 ± 0.0707	-0.14124 ± 0.0707
a3*	0.00157 ± 7.00569E-4	0.00157 ± 7.00569E-4	0.00157 ± 7.00569E-4
a4*	-1.1607E-5 ± 3.5309E-6	-1.1607E-5 ± 3.5309E-6	-1.1607E-5 ± 3.5309E-6
a5*	2.70971E-8 ± 6.37062E-9	2.70971E-8 ± 6.37062E-9	2.70971E-8 ± 6.37062E-9
b0*	24.65341 ± 1.0109	24.65341 ± 1.0109	24.65341 ± 1.0109
b1*	-0.04459 ± 0.025	-0.04459 ± 0.025	-0.04459 ± 0.025
b2*	3.7138E-4 ± 1.17593E-4	3.7138E-4 ± 1.17593E-4	3.7138E-4 ± 1.17593E-4
K	273 ± 0	283 ± 0	298 ± 0
R-Square (COD)	0.99751	0.99885	0.99915
R-Square (COD)*	0.99841		
Adj. R-Square*	0.99823		

Figure S34. C_3H_8 virial fitting (lines) of the adsorption isotherms (points) of LIFM-264 measured at 273 K, 283 K, and 298 K.

,

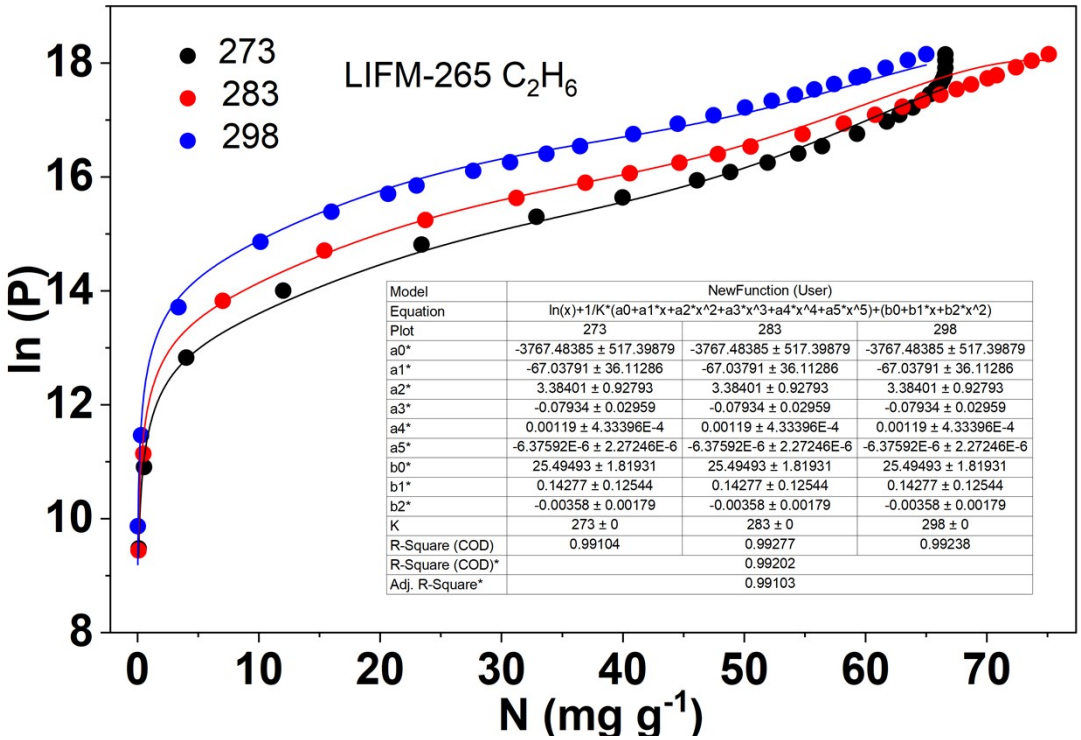

Model	NewFunction (User)		
Equation	ln(x)+1/K*(a0+a1*x+a2*x^2+a3*x^3+a4*x^4+a5*x^5)+(b0+b1*x+b2*x^2)		
Plot	273	283	298
a0*	-3767.48385 ± 517.39879	-3767.48385 ± 517.39879	-3767.48385 ± 517.39879
a1*	-67.03791 ± 36.11286	-67.03791 ± 36.11286	-67.03791 ± 36.11286
a2*	3.38401 ± 0.92793	3.38401 ± 0.92793	3.38401 ± 0.92793
a3*	-0.07934 ± 0.02959	-0.07934 ± 0.02959	-0.07934 ± 0.02959
a4*	0.00119 ± 4.33396E-4	0.00119 ± 4.33396E-4	0.00119 ± 4.33396E-4
a5*	-6.37592E-6 ± 2.27246E-6	-6.37592E-6 ± 2.27246E-6	-6.37592E-6 ± 2.27246E-6
b0*	25.49493 ± 1.81931	25.49493 ± 1.81931	25.49493 ± 1.81931
b1*	0.14277 ± 0.12544	0.14277 ± 0.12544	0.14277 ± 0.12544
b2*	-0.00358 ± 0.00179	-0.00358 ± 0.00179	-0.00358 ± 0.00179
K	273 ± 0	283 ± 0	298 ± 0
R-Square (COD)	0.99104	0.99277	0.99238
R-Square (COD)*	0.99202		
Adj. R-Square*	0.99103		

Figure S35. C_2H_6 virial fitting (lines) of the adsorption isotherms (points) of LIFM-265 measured at 273 K, 283 K, and 298 K.

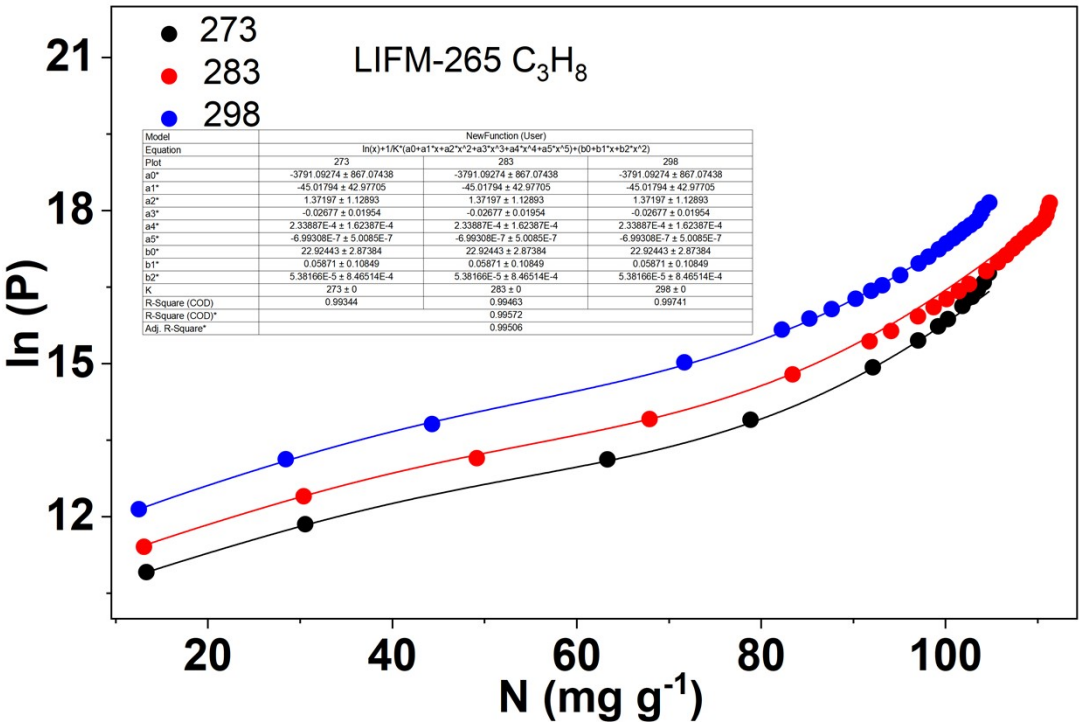

Model	NewFunction (User)		
Equation	ln(x)+1/K*(a0+a1*x+a2*x^2+a3*x^3+a4*x^4+a5*x^5)+(b0+b1*x+b2*x^2)		
Plot	273	283	298
a0*	-3791.09274 ± 867.07438	-3791.09274 ± 867.07438	-3791.09274 ± 867.07438
a1*	-45.01794 ± 42.97705	-45.01794 ± 42.97705	-45.01794 ± 42.97705
a2*	1.37197 ± 1.12893	1.37197 ± 1.12893	1.37197 ± 1.12893
a3*	-0.02677 ± 0.01954	-0.02677 ± 0.01954	-0.02677 ± 0.01954
a4*	2.33887E-4 ± 1.62387E-4	2.33887E-4 ± 1.62387E-4	2.33887E-4 ± 1.62387E-4
a5*	-6.99308E-7 ± 5.0085E-7	-6.99308E-7 ± 5.0085E-7	-6.99308E-7 ± 5.0085E-7
b0*	22.92443 ± 2.87384	22.92443 ± 2.87384	22.92443 ± 2.87384
b1*	0.05871 ± 0.10849	0.05871 ± 0.10849	0.05871 ± 0.10849
b2*	5.38166E-5 ± 8.46514E-4	5.38166E-5 ± 8.46514E-4	5.38166E-5 ± 8.46514E-4
K	273 ± 0	283 ± 0	298 ± 0
R-Square (COD)	0.99344	0.99463	0.99741
R-Square (COD)*	0.99572		
Adj. R-Square*	0.99506		

Figure S36. C_3H_8 virial fitting (lines) of the adsorption isotherms (points) of LIFM-265 measured at 273 K, 283 K, and 298 K.

S7. Comparison of C_3/C_1 IAST Selectivity Enhancing Effects

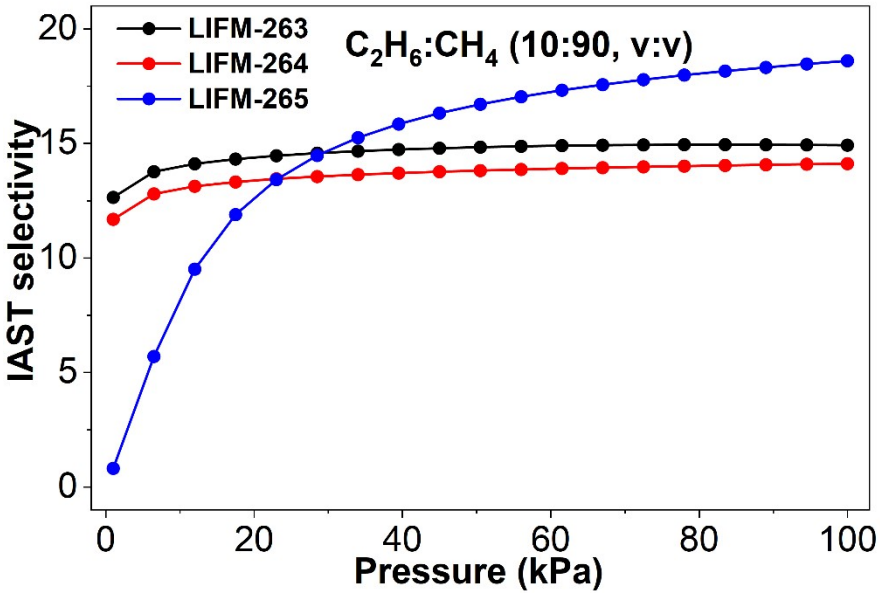

Figure S37. IAST selectivity of the MOFs for C_2H_6/CH_4 (10:90, v:v).

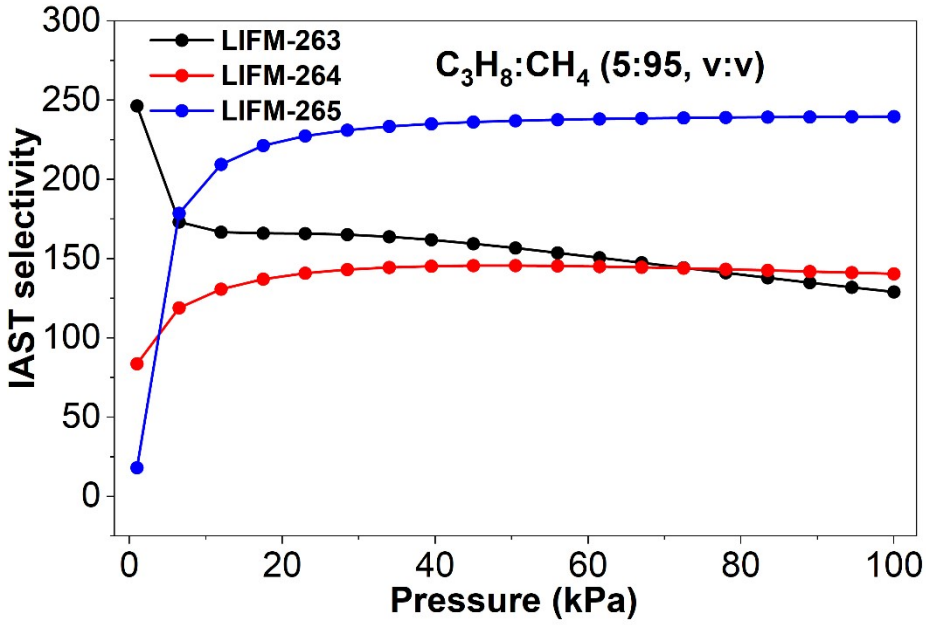

Figure S38. IAST selectivity of the MOFs for C_3H_8/CH_4 (5:95, v:v).

Table S5. $CH_4/C_2H_6/C_3H_8$ adsorption and separation performance for some benchmark adsorbents at 298 K and 100 kPa.

MOFs	CH_4 (mmol g^{-1})	C_2H_6 (mmol g^{-1})	C_3H_8 (mmol g^{-1})	C_2/C_1 IAST selectivity (298K, 50:50)	C_3/C_1 IAST selectivity (298K, 50:50)	Reference
LIFM-263	0.10	0.70	0.76	13	35	This work
LIFM-264	0.12	0.79	1.02	14	95	
LIFM-265	0.09	0.49	0.53	22	256	
ANPC-1-800	1.45	6.84	9.74	14.5	110.4	5
ANPC-2-700	1.12	4.88	8.80	13.5	162.5	
ANPC-2-800	1.15	4.94	11.5	11.9	120.2	
BSF-1	0.66	1.17	0.99	23	353	6
FJI-C4	1.15	2.21	1.63	39.7	293.4	7
FJI-H22	0.88	1.49	1.10	11.95	145.23	8
JLU-Liu5	1.00	2.37	1.59	17.6	107.8	9
JLU-Liu6	0.81	1.63	1.30	20.4	274.6	
JLU-Liu7	1.06	3.57	2.57	50.4	128.5	10
JLU-Liu38	0.48	4.96	8.39	12.5	98	11
JUC-100	0.64	3.07	3.09	11	80	12
JUC-103	0.73	2.85	2.77	8	55	
JUC-106	0.51	2.61	2.59	13	75	
UTSA-35a (296K)	0.43	2.43	2.97	20	80	13
MFM-202a	0.45	4.21	6.76	10	87	14
InOF-1	0.64	4.14	4.25	17	90	15
RT-MIL-100(Fe)	0.36	2.22	6.78	6(10:85)	33.3(5:85)	16
MIL-101-Cr	0.49	1.59	3.35	22.5	84.3	17
MIL-101-Fe	0.45	1.25	3.29	15.4	24.9	
MIL-101-Fe-NH_2	0.46	1.35	3.32	11.6(10:85)	42.5(5:85)	
A-AC-3	1.38	7.09	11.34	16.9(1:4)	76.6(1:4)	18
A-AC-4	1.18	6.59	11.76	15.1(1:4)	88.8(1:4)	
A-AC-5	0.98	5.00	9.12	5.10(Uptake ratio)	9.31(Uptake ratio)	
sPI-A-H	0.39	1.59	2.00	13.3	66.7	19
SBA-15	0.11	0.56	1.24	4.9(Uptake ratio,303K)	/	20

S8. Breakthrough Experiments

Transient breakthrough experiments for the separation of $CH_4/C_2H_6/C_3H_8$ (85:10:5, v:v:v) were carried out in a fixed bed. The column (6 mm inner diameter × 150 mm) was filled with ~1.0 g pre-activated sample for the experiment using a ternary component gases mixture. Before filled in the column, the samples were activated at 373 K for 10 h under vacuum conditions. After filling the column, the column was purged with a He flow for 1 h. The flow rates (5 mL min^{-1} at 298 K and 1 bar) of gases were regulated by mass flow controllers. Then the $CH_4/C_2H_6/C_3H_8$ gas mixture with 5 mL min^{-1} was introduced to the column. The outlet composition was continuously monitored by the mass spectrometer of BSD-MAB multi-constituent adsorption breakthrough curve analyzer until a complete breakthrough was achieved. The sample was regenerated with a He flow (5 mL min^{-1}) at 373 K for 2 h before each cyclic experiment.

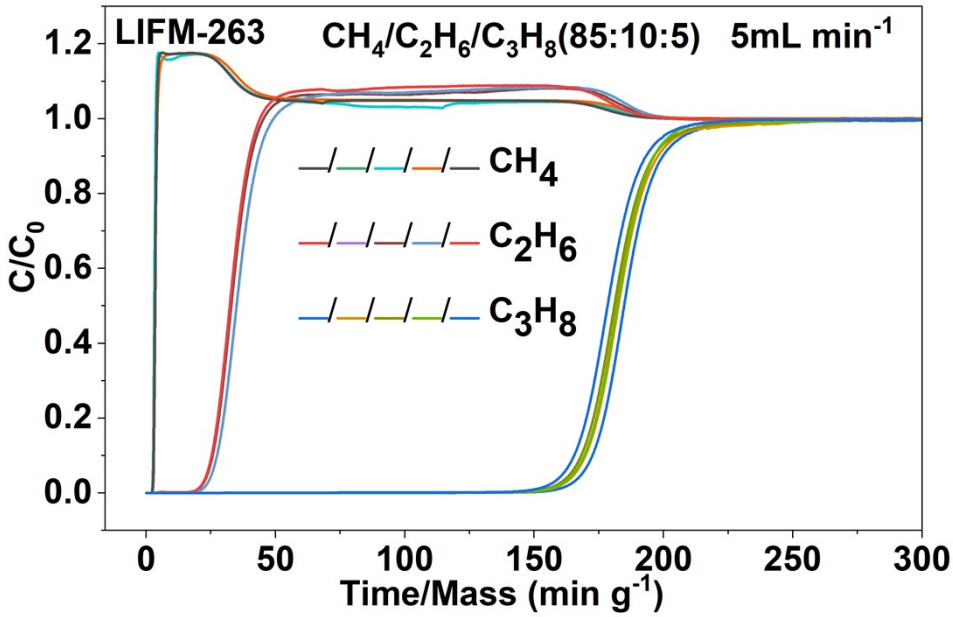

Figure S39. Three cycles of dynamic breakthrough tests of a $CH_4/C_2H_6/C_3H_8$ (85:10:5, v:v:v) mixture for LIFM-263.

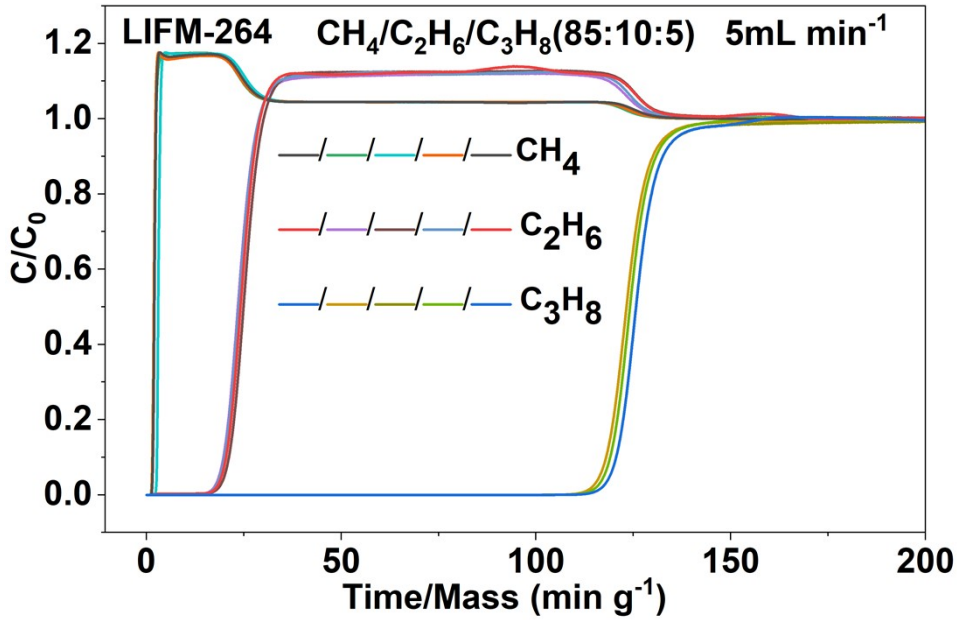

Figure S40. Three cycles of dynamic breakthrough tests of a $CH_4/C_2H_6/C_3H_8$ (85:10:5, v:v:v) mixture for LIFM-264.

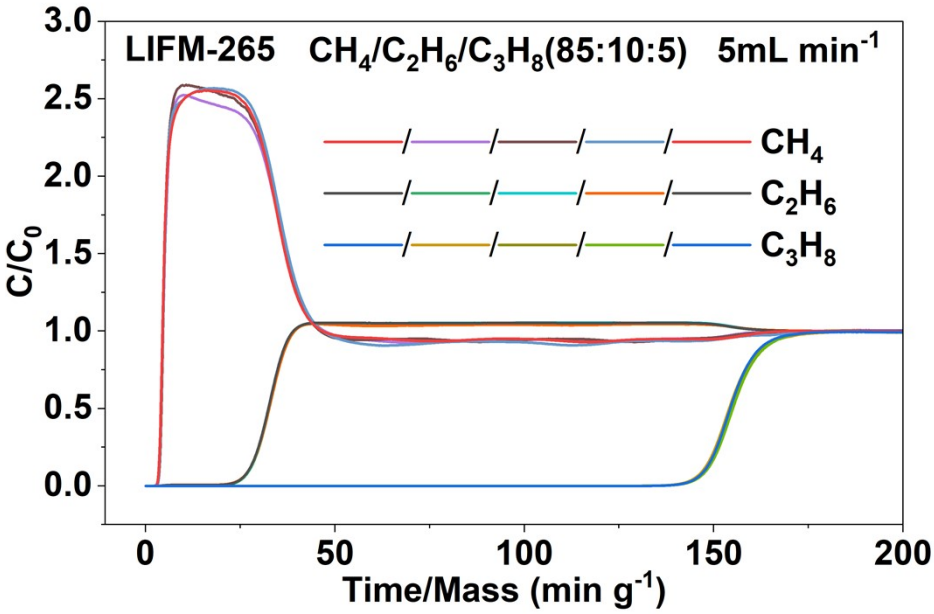

Figure S41. Three cycles of transient breakthrough tests of a $CH_4/C_2H_6/C_3H_8$ (85:10:5, v:v:v) mixture for LIFM-265.

Table S6. Summary of MOF BET surface areas, pore volumes, C_2/C_1 & C_3/C_1 IAST selectivities, isosteric heats (Q_{st}), breakthrough productivities (for CH_4), and breakthrough capture capacities (for C_2H_6 and C_3H_8).

MOF	BET surface area ($m^2\ g^{-1}$)	V_p ($cm^3\ g^{-1}$)	Pore size (nm)	C_2/C_1 IAST selectivity (10: 90 / 50: 50)	C_3/C_1 IAST selectivity (5: 95 / 50: 50)	Q_{st} (kJ mol^{-1})		Breakthrough productivity (mmol g^{-1})	Breakthrough capture capacity (mmol g^{-1})	
						C_2H_6	C_3H_8	CH_4	C_2H_6	C_3H_8
LIFM-263	718	0.30	0.57,0.72	15/13	129/35	23.09	31.93	4.45	0.41	2.39
LIFM-264	1030	0.43	0.57,0.72,1.25	14/14	140/95	23.03	35.65	3.37	0.07	1.41
LIFM-265	763	0.31	0.72	19/ 22	240/256	26.48	34.80	7.92	0.56	1.85

S9. Theoretical Calculations

Grand canonical Monte Carlo (GCMC) calculations were performed with the Sorption module of Materials Studio.[21] One unit cell was used. The MOF structures are all optimized with the Forcite module using Universal force field (UFF). The charges were determined by the charge equilibration (QEq) approach.[22] The structures and charges of CH_4, C_2H_6, and C_3H_8 were prepared with Dmol^3 module (Figure S).[23] The Perdew-Burke-Ernzerhof (PBE) functional was used under the generalized gradient approximation (GGA) functional with the double-ξ numerical polarization (DNP) basis set. The tolerances of energy, gradient, and displacement convergence were 1.0×10^{-5} hartree, 2×10^{-3} hartree $Å^{-1}$, and 5×10^{-3} Å, respectively. The density distribution of the gases on the MOFs were calculated using the fixed pressure task mode of Sorption module under 298K and 100 kPa (CH_4 fugacity: 99.78 kPa; C_2H_6 fugacity: 99.17 kPa; C_3H_8 fugacity: 98.36 kPa). The frameworks were assumed as rigid. DREIDING force field was used and the parameters of Zn and Cd are adopted from Universal force field. A total of 1×10^6 equilibration steps and 1×10^7 production steps were set. The van der Waals interactions were calculated by the atom-based method with a fine cutoff

distance of 18.5 Å, whereas the Coulombic interactions were summed by the Ewald and group method.

The primary binding site and simulated isosteric heat (Q_{st}) values were calculated using the Adsorption Locator module. All the sets are similar to the sorption calculations.

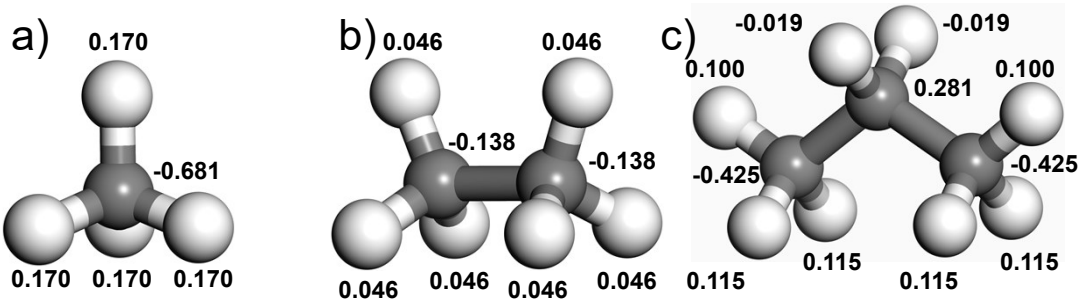

Figure S42. The ESP charges of a) CH_4, b) C_2H_6 and c) C_3H_8.

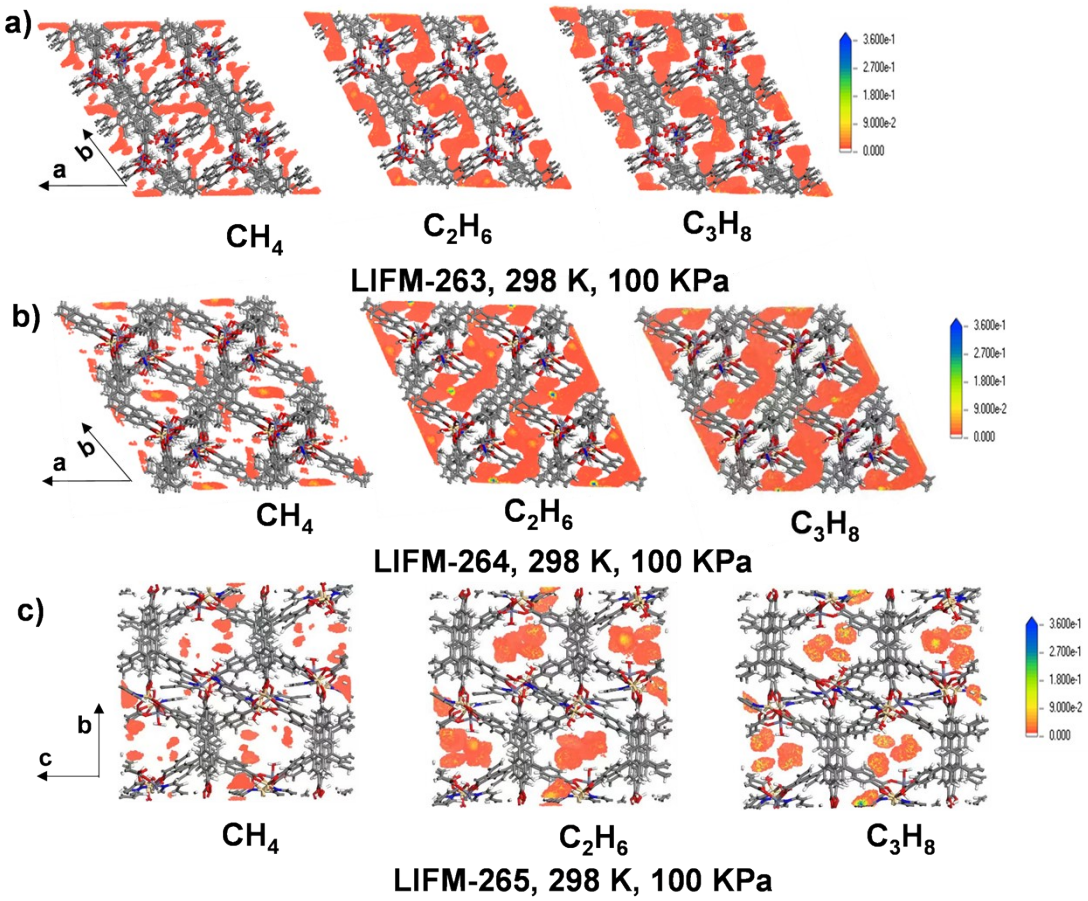

Figure S43. Density distributions of $CH_4/C_2H_6/C_3H_8$ in a) LIFM-263, b) LIFM-264, and c) LIFM-265 under 298K and 100 kPa, respectively.

Table S7. The simulated adsorption capacities (100 kPa), experimental adsorption capacities (100 kPa), calculated Q_{st} at primary adsorption site and experimental Q_{st} at zero coverage of LIFM-263, LIFM-264 and LIFM-265 for $CH_4/C_2H_6/C_3H_8$ adsorption.

MOF	Gas	Simulated adsorption capacities at 100 kPa ($cm^3\ g^{-1}$)	Experimental adsorption capacities at 100 kPa ($cm^3\ g^{-1}$)	Simulated Q_{st} ($kJ\ mol^{-1}$)	Experimental Q_{st} ($kJ\ mol^{-1}$)
LIFM-263	CH_4	15.5	10.5	18.0	-
	C_2H_6	64.7	69.6	26.6	23.1
	C_3H_8	68.9	76.3	36.2	31.9
LIFM-264	CH_4	14.6	12.0	15.2	-
	C_2H_6	73.7	79.0	25.7	23.0
	C_3H_8	79.4	100.0	39.1	35.7
LIFM-265	CH_4	8.4	9.5	17.0	-
	C_2H_6	41.5	48.5	27.8	26.5
	C_3H_8	47.4	53.3	38.1	34.8

S10. References

1. O. V. Dolomanov, L. J. Bourhis, R. J. Gildea, J. A. K. Howard, H. Puschmann, *Journal of Applied Crystallography*. 2009, **42**, 339-341.
2. A. Spek, *Acta Crystallographica Section C-structural Chemistry*. 2015, **71**, 9-18.
3. N. Dutta, G. C. Giri, S. Haldar, G. Vijaykumar, C. D. Stewart, L. Carrella, G. T. Musie and M. Bera, *ChemistrySelect*, 2019, **4**, 10260-10269..
4. V. Machado, M. Turnbull and L. Dawe, *Crystals*, 2018, **8**, 1-8.
5. P. Zhang, X. Wen, L. Wang, Y. Zhong, Y. Su, Y. Zhang, J. Wang, J. Yang, Z. Zeng and S. Deng, *Chemical Engineering Journal*, 2020, **381**, 1-8.
6. Y. Zhang, L. Yang, L. Wang, S. Duttwyler and H. Xing, *Angewandte Chemie International Edition*, 2019, **58**, 8145-8150.
7. L. Li, X. Wang, J. Liang, Y. Huang, H. Li, Z. Lin and R. Cao, *ACS Applied Materials & Interfaces*, 2016, **8**, 9777-9781.
8. P. Huang, C. Chen, F. Jiang, M. Wu and M. Hong, *Crystal Growth & Design*, 2019, **19**, 3103-3108.
9. D. Wang, T. Zhao, Y. Cao, S. Yao, G. Li, Q. Huo and Y. Liu, *Chemical Communications*,

2014, **50**, 8648-8650.
10. J. Luo, J. Wang, Y. Cao, S. Yao, L. Zhang, Q. Huo and Y. Liu, *Inorganic Chemistry Frontiers*, 2017, **4**, 139-143.
11. J. Li, X. Luo, N. Zhao, L. Zhang, Q. Huo and Y. Liu, *Inorganic Chemistry*, 2019, **58**, 11269-11269.
12. J. Jia, L. Wang, F. Sun, X. Jing, Z. Bian, L. Gao, R. Krishna and G. Zhu, *Chemistry – A European Journal*, 2014, **20**, 9073-9080.
13. M. C. Das, H. Xu, S. Xiang, Z. Zhang, H. D. Arman, G. Qian and B. Chen, *Chemistry – A European Journal*, 2011, **17**, 7817-7822.
14. S. Gao, C. G. Morris, Z. Lu, Y. Yan, H. G. W. Godfrey, C. Murray, C. C. Tang, K. M. Thomas, S. Yang and M. Schröder, *Chemistry of Materials*, 2016, **28**, 2331-2340.
15. Y. Chen, Z. Qiao, D. Lv, H. Wu, R. Shi, Q. Xia, H. Wang, J. Zhou and Z. Li, *Industrial & Engineering Chemistry Research*, 2017, **56**, 4488-4495.
16. B. Yuan, X. Wang, X. Zhou, J. Xiao and Z. Li, *Chemical Engineering Journal*, 2019, **355**, 679-686.
17. L.-Z. Qin, X.-H. Xiong, S.-H. Wang, L. Zhang, L.-L. Meng, L. Yan, Y.-N. Fan, T.-A. Yan, D.-H. Liu, Z.-W. Wei and C.-Y. Su, *ACS Applied Materials & Interfaces*, 2022, **14**, 45444-45450.
18. W. Liang, H. Xiao, D. Lv, J. Xiao and Z. Li, *Separation and Purification Technology*, 2018, **190**, 60-67.
19. J. Yan, B. Zhang and Z. Wang, *ACS Applied Materials & Interfaces*, 2018, **10**, 26618-26627.
20. B. L. Newalkar, N. V. Choudary, P. Kumar, S. Komarneni and T. S. G. Bhat, *Chemistry of Materials*, 2002, **14**, 304-309.
21. M. Eddaoudi, D. F. Sava, J. F. Eubank, K. Adil and V. Guillerm, *Chemical Society Reviews*, 2015, **44**, 228-249.
22. L. Gong, Y. Ye, Y. Liu, Y. Li, Z. Bao, S. Xiang, Z. Zhang and B. Chen, *ACS Applied Materials & Interfaces*, 2022, **14**, 19623-19628.
23. M. Fischer, F. Hoffmann and M. Fröba, *ChemPhysChem*, 2010, **11**, 2220-2229.